

Ph.D. Thesis

**Probing Electroweakly Interacting
Massive Particles
with Drell-Yan Process
at 100 TeV Colliders**

So Chigusa

Department of Physics



THE UNIVERSITY OF TOKYO

December 2019

Abstract

(♣ To be written ♣)

Acknowledgments

(♣ To be written ♣)

Contents

1	Introduction	1
2	Models with WIMPs	2
2.1	Minimally supersymmetric standard model	2
2.2	Minimal dark matter model	11
2.3	Summary	14
3	WIMP as a dark matter	16
3.1	WIMP dark matter relic abundance	16
3.2	WIMP DM search : indirect detection	19
3.3	WIMP DM search : direct detection	19
3.4	Need review	19
4	Direct collider search of WIMPs	21
4.1	WIMP production	21
4.2	Disappearing track search	26
4.3	Soft lepton search	27
4.4	Mono-jet search	27
5	Probing EWIMPs with Drell-Yan process at 100 TeV colliders	28
5.1	EWIMP effect on the lepton production processes	28
5.2	Analysis	32
5.2.1	Event generation	32
5.2.2	Statistical treatment	33
5.2.3	Detection reach	37
5.2.4	Determination of EWIMP properties	39
5.3	Conclusion	43
	Appendix A Review of supersymmetry	45

Section 1

Introduction

- (♣ Unit: $\hbar = c = k_B = 1$ and definition of g_1 and etc? ♣)
- (♣ Definition of Feynmann Slash ♣)
- (♣ Definition of σ matrices ♣)
- (♣ Convention: dot as time derivative ♣)
- (♣ Definition of “SM” ♣)
- (♣ Definition of “WIMP” ♣)
- (♣ Definition of “DM” ♣)

Section 2

Models with WIMPs

There are several examples of the models that contain WIMP DM candidates. In this section, two of them (**♣ Really? ♣**) are briefly reviewed. (**♣ EWIMP and WIMP?? ♣**)

2.1 Minimally supersymmetric standard model

(**♣ Summary of SUSY particle names somewhere ♣**)

The minimally supersymmetric standard model (MSSM) is the simple extension of the SM with $\mathcal{N} = 1$ supersymmetry (SUSY).^{‡1} One of the motivations to introduce SUSY is to solve the so-called hierarchy (or naturalness) problem [1–3] in the SM. The problem is related to the quantum correction to the SM Higgs boson mass from heavy new physics particles. For example, we can consider the one-loop correction to the Higgs mass from a Weyl fermion f and a complex scalar S as illustrated in Fig. 1. The corrections to the Higgs mass is given by

$$\Delta m_h^2 = -\frac{|\lambda_f|^2}{8\pi^2} \left[\Lambda_{\text{UV}}^2 - 2m_f^2 \ln \left(\frac{\Lambda_{\text{UV}}}{m_f} \right) + \dots \right] \quad (\text{fermion}), \quad (2.1)$$

$$\Delta m_h^2 = \frac{\lambda_S}{16\pi^2} \left[\Lambda_{\text{UV}}^2 - 2m_S^2 \ln \left(\frac{\Lambda_{\text{UV}}}{m_S} \right) + \dots \right] \quad (\text{scalar}), \quad (2.2)$$

(**♣ Check this! ♣**) where λ_f and m_f are the Higgs-fermion coupling constant and the fermion mass, respectively, and λ_S and m_S are those for the scalar S . We take the cut-off

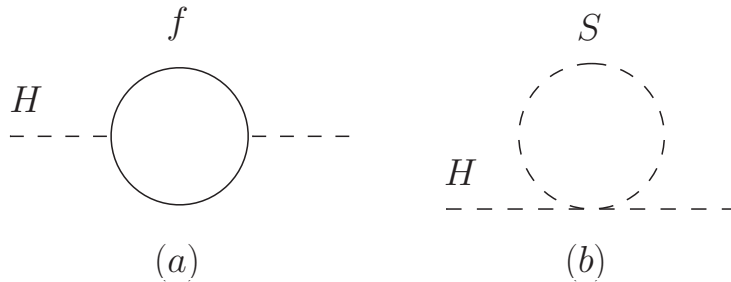


Figure 1: One-loop correction to the Higgs mass from (a) a Weyl fermion f and (b) a complex scalar S .

^{‡1}For a brief review of the $\mathcal{N} = 1$ SUSY, see Sec. A.

Notation	$SU(3)_C$	$SU(2)_L$	$U(1)_Y$
\hat{Q}_i	3	2	1/6
\hat{L}_i	1	2	-1/2
\hat{U}_i	$\bar{3}$	1	-2/3
\hat{D}_i	$\bar{3}$	1	1/3
\hat{E}_i	1	1	1
\hat{H}_u	1	2	1/2
\hat{H}_d	1	2	-1/2

Table 1: Notations and quantum numbers of the chiral superfields in the MSSM.

Notation	$SU(3)_C$	$SU(2)_L$	$U(1)_Y$
\hat{g}	8	1	0
\hat{W}	1	3	0
\hat{B}	1	1	0

Table 2: Notations and quantum numbers of the vector superfields in the MSSM.

scale of the theory to be Λ_{UV} to regularize the otherwise divergent loop integral and neglect the lower order terms of Λ_{UV} . Eqs. (2.1) and (2.2) show the quadratic dependence of Δm_H^2 on Λ_{UV} , which means that the Higgs mass is sensitive to the energy scale of the beyond the SM physics. However, there is at least one extremely high energy scale physics in the nature, gravity at the Planck scale $M_{\text{pl}} \sim 10^{18-19}$ GeV. By substituting $\Lambda_{UV} = M_{\text{pl}}$ in Eqs. (2.1) and (2.2) and assuming $\lambda_f \sim \lambda_S \sim \mathcal{O}(1)$, we notice that orders-of-magnitude fine-tuning is required to obtain the correct Higgs mass $m_h = 125.10$ GeV [4], which is unnatural.

SUSY provides a nice solution to this fine-tuning problem. As is summarized in Appendix A, (**♣ summarize later ♣**) each Weyl fermion in a supersymmetric model has two complex scalars with the same mass $m_f = m_S$. In addition, their coupling constants should have a relationship $|\lambda_f|^2 = \lambda_S$ due to the fact that λ_S is a coupling constant in the F-term potential sourced by a superpotential term proportional to λ_f . (**♣ description of F-term and D-term ♣**) By using both equations and summing the corrections (2.1) and (2.2) with factor of two multiplied to the latter, we obtain a result independent of the cut-off scale Λ_{UV} without fine-tuning. This cancellation is ensured by the so-called non-renormalization theorem. [5, 6]

We now summarize the notations and quantum numbers of the chiral and vector superfields in the MSSM in Table 1 and 2, respectively. The supersymmetric part of the MSSM

lagrangian is described by the superpotential ^{‡2}

$$W = Y_u^{ij} \hat{U}_i \hat{Q}_j \hat{H}_u - Y_d^{ij} \hat{D}_i \hat{Q}_j \hat{H}_d - Y_e^{ij} \hat{E}_i \hat{L}_j \hat{H}_d + \mu \hat{H}_u \hat{H}_d, \quad (2.3)$$

where $i, j = 1, 2, 3$ labels the quark and lepton generation, while Q, L, U, D, E are superfields that contain the left-handed quark, left-handed lepton, right-handed up-type quark, right-handed down-type quark, and right-handed charged lepton, respectively. In Eq. (2.3), proper contraction of $SU(3)_C$ and $SU(2)_L$ indices is assumed. Note that two Higgs doublets H_u and H_d with opposite values of $U(1)_Y$ hypercharges are introduced, which is needed to cancel the contributions to the gauge anomaly from fermionic partners of the Higgs doublets.

Postulating SM gauge symmetries as a unique guideline to construct a model, there are a few more terms allowed in the superpotential:

$$W_{\Delta L=1} = \lambda^{ijk} \hat{L}_i \hat{L}_j \hat{E}_k + \lambda'^{ijk} \hat{L}_i \hat{Q}_j \hat{D}_k + \mu^i \hat{L}_i \hat{H}_u, \quad (2.4)$$

$$W_{\Delta B=1} = \lambda''^{ijk} \hat{U}_i \hat{D}_j \hat{D}_k. \quad (2.5)$$

Terms in Eqs. (2.4) and (2.5) are phenomenologically problematic since they lead to the lepton and baryon number violating operators, respectively, which may cause a too fast proton decay, depending on parameters (see for example [8]). To avoid this problem, we often rely on a symmetry called the R-parity [9] or the matter parity [8, 10–12]. Charges of the R-parity, which is basically a Z_2 symmetry, are calculated as

$$P_R = (-1)^{3(B-L)+2s}, \quad (2.6)$$

where B, L , and s are the baryon number, lepton number, and spin of the particle, respectively. According to the definition, we can see that all the SM particles have even parity ($P_R = +1$), while all the supersymmetric particles have odd parity ($P_R = -1$). Then it is easy to check that Eqs.(2.4) and (2.5) lead to the R-parity violating terms in the Lagrangian and thus are forbidden, while all the terms in Eq. (2.3) remain allowed. From now on, we only focus on the R-parity conserving MSSM.

Since no superpartner of any SM particle is observed yet, SUSY should be broken and superpartners should obtain the SUSY breaking masses. (**♣ ref: boson and fermion obtain equal mass ♣**) The SUSY breaking part of the lagrangian is expressed as

$$\begin{aligned} \mathcal{L}_{\text{soft}} = & -\frac{1}{2} \left(M_3 \tilde{g} \tilde{g} + M_2 \tilde{W} \tilde{W} + M_1 \tilde{B} \tilde{B} + \text{c.c.} \right) \\ & - \left(A_u^{ij} \tilde{U}_i \tilde{Q}_j \tilde{H}_u - A_d^{ij} \tilde{D}_i \tilde{Q}_j \tilde{H}_d - A_e^{ij} \tilde{E}_i \tilde{L}_j \tilde{H}_d \right) \\ & - m_Q^{2ij} \tilde{Q}_i^\dagger \tilde{Q}_j - m_L^{2ij} \tilde{L}_i^\dagger \tilde{L}_j - m_U^{2ij} \tilde{U}_i^\dagger \tilde{U}_j - m_D^{2ij} \tilde{D}_i^\dagger \tilde{D}_j - m_E^{2ij} \tilde{E}_i^\dagger \tilde{E}_j \\ & - m_{H_u}^2 H_u^* H_u - m_{H_d}^2 H_d^* H_d - (b H_u H_d + \text{c.c.}), \end{aligned} \quad (2.7)$$

^{‡2}For a more detailed review of the MSSM, see for example [7].

where the tilde is used to express the superpartner of the SM particle contained in a superfield, while a field without a hat nor tilde denotes the other component. An exception is two Higgs doublets, where H_u and H_d express the scalar components, while \tilde{H}_u and \tilde{H}_d express their superpartners called Higgsinos. The SM-like Higgs doublet H corresponds to a linear combination of H_u and H_d .

It is known that, within the MSSM, almost all SUSY breaking mechanisms, such as the F-term (O’Raifeartaigh) [13] or D-term (Fayet-Iliopoulos) SUSY breaking [14, 15], fail to generate masses of superpartners with remaining the SM gauge group in the low energy effective theory. Thus, we need a so-called hidden sector in addition to the MSSM sector, in which SUSY is spontaneously broken. In order for the MSSM sector to have Lagrangian terms (2.7), we also need some mediation mechanism of the SUSY breaking. The relative size of the SUSY breaking parameters in Eq. (2.7) highly depends on the mediation mechanism. Among many mediation mechanisms of SUSY breaking, the anomaly mediated SUSY breaking [16, 17] leads to an interesting phenomenology with relatively light WIMPs, so it will be reviewed later.

Dark matter candidate in the MSSM

There is another motivation to consider the (R-parity preserving) MSSM: the existence of the DM. Since there is a sizable amount of DM in the current universe, a DM candidate should be stable or have sufficiently small decay width. In many models, the stability of DM is ensured by imposing a symmetry and/or by kinematically forbidding the DM decay. In the MSSM, the role of stabilizer can be played by the R-symmetry described above. Recalling that all the SM (supersymmetric) particles have even (odd) parity, each interaction vertex in the MSSM Lagrangian should contain an even number of supersymmetric particles. If we consider the lightest supersymmetric particle (LSP), such vertices can not construct the kinematically allowed LSP decay chain and, as a result, the LSP becomes a stable DM candidate.

The DM phenomenology, such as the production and annihilation of DM in the universe and processes that allow us to efficiently detect it, highly depends on which species of supersymmetric particle becomes the LSP. Hereafter, we only focus on the cases where one of the gauginos and Higgsinos becomes the LSP with some motivations described below. In addition, all the LSP candidates to be described have non-zero electroweak charges and they can be viewed as examples of the WIMPs.

Higgs mass in the MSSM

Under the spontaneously broken SUSY, the cancellation of the quantum correction to the Higgs boson discussed above is not exact. One obvious consequence of the SUSY breaking

Value	Description	Reference
$M_W = 80.384 \pm 0.014 \text{ GeV}$	Pole mass of the W boson	[18, 19]
$M_Z = 91.1876 \pm 0.0021 \text{ GeV}$	Pole mass of the Z boson	[20]
$M_h = 125.15 \pm 0.24 \text{ GeV}$	Pole mass of the Higgs	[21, 22]
$M_t = 173.34 \pm 0.82 \text{ GeV}$	Pole mass of the top quark	[23]
$(\sqrt{2}G_\mu)^{-1/2} = 246.21971 \pm 0.00006 \text{ GeV}$	Fermi constant for μ decay	[24]
$\alpha_3(M_Z) = 0.1184 \pm 0.0007$	$\overline{\text{MS}}$ $SU(3)_C$ gauge coupling	[25]

Table 3: Experimentally measured SM parameters used for the derivation of Eq. (2.9).

in Eqs. (2.1) and (2.2) is the hierarchy between m_f and m_S that appear in the second term of each contribution. In the case of the MSSM, the largest contribution comes from the superpartner of the top quark, stop, that have the largest Yukawa coupling with the Higgs boson.

When there is a large hierarchy between the SUSY breaking scale M_S , which is comparable with stop masses, and the top mass M_t , the stop contributions to the Higgs mass contains a large logarithm of the form of $\log(M_S^2/M_t^2)$. (**♣ Consistency with above equations. Maybe MSbar better ♣**) To resum this large logarithm and obtain a precise result, we have to rely on the renormalization group equation (RGE). In this framework, the value of the Higgs self coupling λ at the electroweak scale is closely related to the Higgs mass. We assume the SM parameters summarized in Table 3 and the definition of the SM Higgs potential

$$V(H) = -\frac{m^2}{2}|H|^2 + \lambda|H|^4, \quad (2.8)$$

with H being the SM Higgs doublet. Then, according to [26], we obtain the relationship ^{‡3}

$$\lambda(M_t) = 0.12604 + 0.00206 \left(\frac{M_h}{\text{GeV}} - 125.15 \right) - 0.00004 \left(\frac{M_t}{\text{GeV}} - 173.34 \right), \quad (2.9)$$

where the $\overline{\text{MS}}$ scheme is used to renormalize the divergence of loop integrals.

In the MSSM, the value of λ at the SUSY breaking scale M_S is given by

$$\lambda(M_S) = \frac{g_1^2(M_S) + g_2^2(M_S)}{8} \cos^2 2\beta + \delta\lambda, \quad (2.10)$$

^{‡3}Although the values listed in Table 3 are different from the latest ones given in [4], we use older ones because the change in input values may cause the slight change in coefficients of second and third terms of Eq. (2.9). The latest central values of the Higgs and top masses are $M_h = 125.10 \text{ GeV}$ and $M_t = 173.1 \text{ GeV}$, with which we can estimate $\lambda(M_t) = 0.12595$.

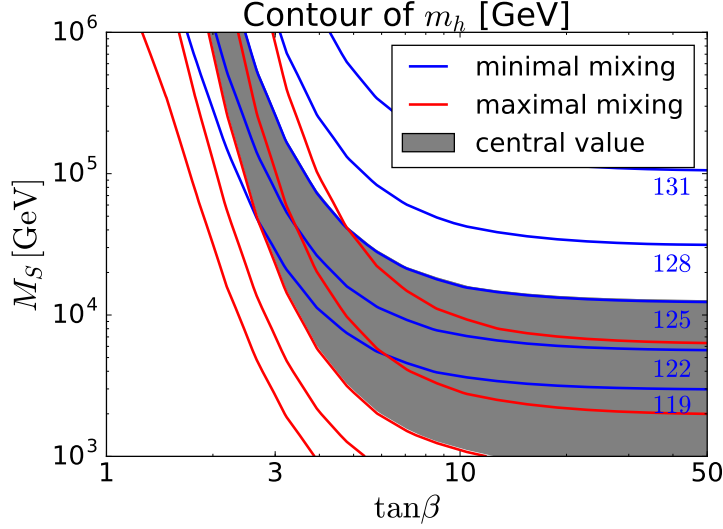


Figure 2: Contour of the Higgs mass m_h in the $\tan\beta$ vs. M_S plane. The universal mass M_S is assumed for all the SUSY particles. Blue (red) lines correspond from top to bottom to the contours of $m_h = 131, 128, 125, 122, 119$ GeV for the minimal (maximal) stop mixing. Gray shade corresponds to the region where $m_h = 125.10$ GeV can be explained.

where g_1 and g_2 are $U(1)_Y$ and $SU(2)_L$ gauge coupling constants, respectively, while β parametrizes the ratio of the vacuum expectation values

$$\frac{\langle H_u^0 \rangle}{\langle H_d^0 \rangle} = \tan\beta, \quad (2.11)$$

with H_u^0 and H_d^0 being electromagnetically neutral components of the corresponding Higgs doublets. In Eq. (2.10), the first term shows the tree-level contribution from the D-term potential and $\delta\lambda$ denotes the threshold correction from heavy superpartners. M_S is often chosen to be the geometric mean of stop masses to minimize the largest contribution to $\delta\lambda$ from stops. Once the spectrum of the MSSM particles is fixed, we can evaluate the Higgs self coupling using Eq. (2.10), calculate its running according to the RGE, and obtain the prediction for the Higgs mass through Eq. (2.9).

In Fig. 2, we show the contour plot of the Higgs mass m_h in the $\tan\beta$ vs. M_S plane. We assume the universal mass M_S for all the SUSY particles. Under this assumption, the largest contribution to the threshold correction $\delta\lambda$ from stops can be written as

$$\delta\lambda \simeq \frac{9y_t^2(M_S)}{16\pi^2} \tilde{X}_t \left[1 - \frac{\tilde{X}_t}{12} \right], \quad (2.12)$$

$$\tilde{X}_t \equiv \frac{(A_t - \mu \cot\beta)^2}{M_S^2}, \quad (2.13)$$

with $y_t \equiv Y_u^{33}$ and $A_t \equiv A_u^{33}$. It is obvious from Eq. (2.12) that, for a moderate value of $\tilde{X}_t \lesssim \mathcal{O}(1)$, $\tilde{X}_t = 0$ ($\tilde{X}_t = 6$) corresponds to the case with minimum (maximum) threshold correction, often called as the minimal (maximal) stop mixing. ^{‡4}

The red (blue) lines in Fig. 2 denote from top to bottom the contours of $m_h = 131, 128, 125, 122, 119$ GeV for the minimal (maximal) stop mixing. Gray shade corresponds to the region where the central value of the observation $m_h = 125.10$ GeV can be explained. From the figure, we can see that the discovery of the Higgs with $m_h = 125.10$ GeV may indicate a somewhat heavy SUSY breaking scale $M_S \gtrsim 10$ TeV for the case with a small stop mixing or a small $\tan \beta$. Combined with the fact that there is still no sign of the superpartners at the collider experiment, this motivates us to consider a heavy SUSY scenario.

Light Higgsino and its relation to the naturalness

When we consider a heavy SUSY model in relation to the Higgs mass, there is another problem called the little hierarchy problem. This mentions the hierarchy between the electroweak scale and the heavy SUSY breaking scale and an accompanying fine-tuning. Although the degree of the required fine-tuning is several orders of magnitude smaller than that for the large hierarchy between the electroweak and Planck scales, it will be more acceptable if some mechanism relieves the fine-tuning. The problem can be summarized in the equation

$$\frac{1}{2}m_Z^2 = \frac{m_{H_d}^2 - m_{H_u}^2 \tan^2 \beta}{\tan \beta^2 - 1} - \mu^2, \quad (2.14)$$

where the right-handed side is the MSSM prediction for the Z -boson mass assuming the successful electroweak symmetry breaking. If some of the MSSM parameters m_{H_d} , m_{H_u} , μ are much larger than m_Z , there should be some amount of fine-tuning to satisfy the equation.

There is a measure of the fine-tuning in this sense, proposed in [27, 28]:

$$\Delta_{a_i} \equiv \frac{a_i}{m_Z^2} \frac{\partial m_Z^2}{\partial a_i}, \quad (2.15)$$

where a_i is a MSSM model parameter. In order for the model to be “natural”, we require $|\Delta_{a_i}| < \Delta$ for any a_i with a typical choice of $\Delta \sim \mathcal{O}(10-100)$. (**♣ Typical?? ♣**) Since m_Z is sensitive to the Higgsino mass μ , this gives an upper bound on the “natural” choice of the Higgsino mass

$$\mu^2 < \frac{m_Z^2}{2} \Delta, \quad (2.16)$$

^{‡4}Eq. (2.12) shows that $\delta\lambda < 0$ for $\tilde{X}_t > 12$, resulting in the prediction of a lighter Higgs mass than the minimal stop mixing case. However, the parameter space with $\tilde{X}_t \gtrsim 6$ is severely constrained by the requirement of the stability of the electroweak vacuum (**♣ Reference!! ♣**) and is not considered here.

predicting the (sub-)TeV scale Higgsino. As we will see in Sec. ??, (**♣ Caution!! ♣**) this light Higgsino is also fascinating as a dark matter candidate.

Even when the SUSY breaking scale is much higher than the electroweak scale, it is not strange for Higgsino to be around the electroweak scale since it is protected by an R-symmetry and a Peccei Quinn symmetry. (**♣ Reference!! ♣**) This symmetry protection is also important for a solution to the so-called “ μ -problem” [29], where the large hierarchy between the SUSY conserving parameter μ and the cut-off scale of the MSSM itself is discussed. When we consider the low energy effective field theory in which SUSY is broken and all the squarks and sleptons are decoupled, a unique linear combination of the R-symmetry and the Peccei Quinn symmetry is enhanced only if both gauginos and Higgsinos are massless. This fact leads to the framework of the split SUSY [30], in which there is a hierarchy between the masses of Higgsinos / gauginos and the other SUSY particles. In this framework, the phenomenology highly depends on the ordering and hierarchy of Higgsino and gaugino masses. In particular, the phenomenology of Higgsino will be summarized in Sec. ??? (**♣ Caution!! ♣**) for the case when gauginos are heavier than Higgsino.

Finally, the naturalness requirement discussed above also impose an upper bound on other parameters, in particular on $m_{H_u}^2$ for $\tan^2 \beta \gg 1$. The small value of $m_{H_u}^2$ can be realized by the focus point mechanism [31–33], where the choice of the SM parameters in our universe, in particular that of y_t , allows $m_{H_u}^2$ at the low energy scale to be insensitive to its boundary condition at the high energy scale.

(**♣ Dirac nature of Higgsino? ♣**)

Light Wino in the anomaly mediated SUSY breaking model

Among many mediation models compatible with the heavy SUSY, the anomaly mediated SUSY breaking [16, 17] or the pure gravity mediation scenario [34–36] is of particular interest since it naturally predicts the existence of WIMPs (basically Winos denoted as \tilde{W}) in the TeV range. In this scenario, the SUSY breaking effect is directly mediated to the quark and lepton supermultiplets, and they obtain masses comparable to the scale of the SUSY breaking, which is approximated by the gravitino mass $m_{3/2}$. Higgsino is also consider to be heavy contrary to the model described above. Actually, It is easy to realize the hidden sector dynamics that generates the μ -term of $\mathcal{O}(m_{3/2})$. On the other hand, the superpartners of gauge bosons, gauginos, is affected only through a one-loop diagram, which is related to the conformal anomaly. As a result, gaugino mass parameters in Eq. (2.7) are one-loop suppressed compared with other mass parameters as

$$M_i(M_S) = - \left. \frac{\beta_i}{2g_i^2} \right|_{M_S} m_{3/2}, \quad (2.17)$$

where $i = 1, 2, 3$ is a gauge index and β_i denote the beta functions of gauge coupling constants. (**♣ All-order expression or not? M_S ? M_{GUT} ? ♣**) At the one-loop level, this gives

$$M_1(M_S) = \frac{11g_1^2(M_S)}{16\pi^2}m_{3/2}, \quad (2.18)$$

$$M_2(M_S) = \frac{g_2^2(M_S)}{16\pi^2}m_{3/2}, \quad (2.19)$$

$$M_3(M_S) = -\frac{3g_3^2(M_S)}{16\pi^2}m_{3/2}. \quad (2.20)$$

(♣ Normalization of g_1 ? ♣)

Since Higgsinos are assumed to have a mass comparable to $m_{3/2} \sim M_S$, they decouple from the effective theory below the scale M_S . To take account of the correction to the gaugino masses from the Higgs-Higgsino loop, one has to include the threshold correction at M_S

$$\Delta M_1 = \frac{g_1^2(M_S)}{16\pi^2}L, \quad \Delta M_2 = \frac{g_2^2(M_S)}{16\pi^2}L, \quad (2.21)$$

with

$$L \equiv \mu \sin 2\beta \frac{m_A^2}{|\mu|^2 - m_A^2} \ln \frac{|\mu|^2}{m_A^2}, \quad (2.22)$$

where m_A is the mass of the heavy CP-odd Higgs which is given by a linear combination of H_u^0 and H_d^0 .

Below M_S , gaugino mass parameters further run towards the gaugino mass scale $M_{\tilde{G}}$, where the physical gaugino masses are determined. Note that the bino and wino masses are roughly given by $|M_1(M_{\tilde{G}})|$ and $M_2(M_{\tilde{G}})$, while the gluino pole mass $m_{\tilde{g}}$ includes a sizable effect from the threshold correction as [30]

$$m_{\tilde{g}} = |M_3(M_{\tilde{G}})| \left[1 + \frac{g_3^2}{16\pi^2} \left(12 + 9 \ln \frac{M_{\tilde{G}}^2}{|M_3|^2} \right) \right]. \quad (2.23)$$

The gaugino scale is often defined through $M_3(M_{\tilde{G}}) = M_{\tilde{G}}$ to minimize the size of the logarithmic term in Eq. (2.23).

In Fig. 3, we show the dependence of gaugino masses on $m_{3/2}$ and L . In the left panel, we take $\tan \beta = 2.5$ and $L = 0$, and the $m_{3/2}$ dependence is shown. Blue, green, and red lines denote the masses of Bino, Wino, and gluino, respectively. We can see that, throughout the parameter region used here, Wino becomes the lightest gaugino, or the LSP that can be a dark matter candidate. In this choice of parameters, $m_{3/2} = 10^6 \text{ GeV}$ roughly corresponds to the observed value of the Higgs mass $m_h \sim 125 \text{ GeV}$, which at the same time realizes

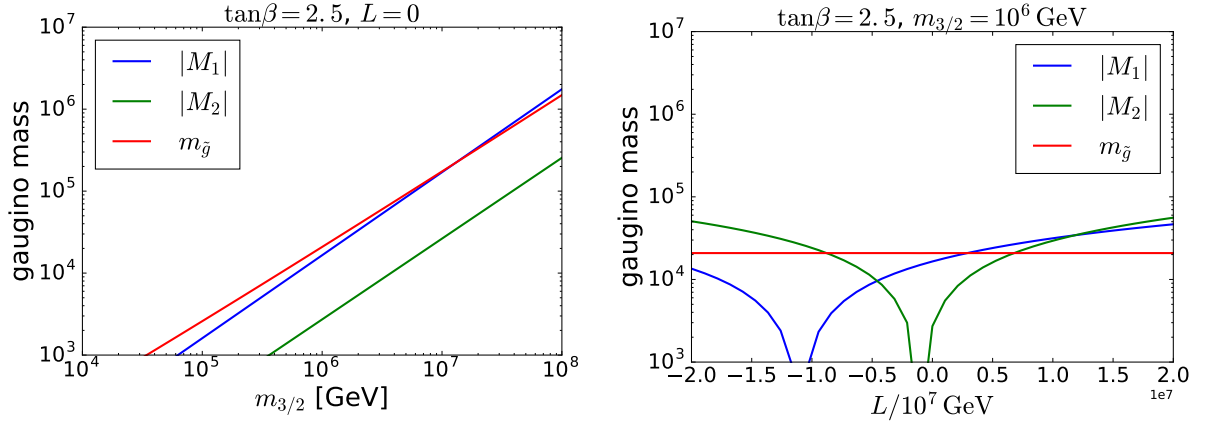


Figure 3: Gaugino masses as a function of $m_{3/2}$ with fixing $L = 0$ (left) and that of L with fixing $m_{3/2} = 10^6$ GeV (right). Blue, green, and red lines denote the masses of Bino, Wino, and gluino, respectively. $\tan\beta = 2.5$ is used in both figures.

the $\mathcal{O}(1)$ TeV mass for Wino. As we will see in Sec. ??, (**♣ Caution!! ♣**) the Wino dark matter in this mass range is well-motivated since it gives us a collect relic abundance of the dark matter.

In the right panel of Fig. 3, we also show the L dependence of gaugino masses for $\tan\beta = 2.5$ and $m_{3/2} = 10^6$ GeV. For simplicity, we neglect the relative phase of $m_{3/2}$ and L and only consider the relative sign of them. It can be seen that the hierarchy between gaugino masses is changed when a large value of $|L|$ is considered. However, we can safely say that when the threshold correction is sufficiently small, $|L| \lesssim \mathcal{O}(m_{3/2})$, Wino remains to be the LSP. In addition, dependence of m_h on L is negligibly small and m_h changes only $\mathcal{O}(0.1)$ GeV within the parameter choice of the right panel.

(**♣ Majorana nature of Wino? ♣**)

2.2 Minimal dark matter model

The minimal dark matter (MDM) [37–39] is another example model that contains a WIMP DM candidate. This model attempts to explain the existence of the stable DM by extending the SM as simply as possible. More specifically, we just assume the same gauge groups as the SM and add only one $SU(2)_L$ n -plet with/without $U(1)_Y$ hypercharge Y in the model.^{b5} Y is chosen such that one component of the multiplet, after the electroweak symmetry breaking, has no $U(1)_{\text{EM}}$ charge, and thus can be a DM candidate. This condition leaves

^{b5}This new particle, when it is a fermion, does not contribute to the $SU(2)_L^2 U(1)_Y$, $U(1)_Y^3$, nor $U(1)_Y \text{grav}^2$ anomalies if $Y = 0$. When $Y \neq 0$, we always consider a vector-like pair of Weyl fermions, which as a whole consists of a Dirac fermion and cancels the contributions to the gauge anomalies.

only n discrete choices of Y for an $SU(2)_L$ n -plet.

In the $SU(2)_L$ limit, masses of all the components in the multiplet are the same. Since $SU(2)_L$ symmetry is spontaneously broken, the mass difference among them is generated at one-loop level and a heavy component can decay into a lighter component. In order for the multiplet to explain the DM in the current universe, the $U(1)_{\text{EM}}$ neutral component should have the lowest mass. We will return to this point and check that this is the case in Sec. ??? **(♣ Caution!! ♣)**, related to the collider search for MDMs using the disappearing track signal.

In some sence, the MDM is just a generalization of the WIMP described above. Actually, if we choose the set of $SU(2)_L$ and $U(1)_Y$ charges as $(n, Y) = (2, \pm 1/2)$ and $(3, 0)$, they correspond to the Higgsino and Wino, respectively. However, for these choices, the stability of the $U(1)_{\text{EM}}$ neutral component is not automatically ensured, and some extra symmetry (in this case the R-parity) is needed for the DM to survive until now. The important point of the new framework MDM is that, when we use large $n \geq 5$, there are examples of multiplets that automatically contain a sufficiently long-lived DM candidate.

The stability of such multiplets can be understood through a simple group theoretical argument. To write down the effective operator that describes the decay of a n -plet field to SM particles, we have to make a n -plet representation out of several SM fields. However, since the largest $SU(2)_L$ representation in the SM is doublet, we need at least $n - 1$ SM fields in the operator. The operator made out of this large number of fields should be suppressed by a power of the cutoff scale Λ , at least by Λ^{4-n} (Λ^{3-n}) for a scalar (fermion) MDM, and results in a small decay rate. Since the well-motivated DM mass is of $\mathcal{O}(\text{TeV})$ as we will see in Sec. ?? **(♣ Caution!! ♣)**, the resulting lifetime of the DM candidate is estimated as $\tau \sim \Lambda^{-2p}(\text{TeV})^{2p-1}$ for an operator with a suppression factor Λ^{-p} . By demanding τ to be larger than the age of the universe under the assumption for the cut off scale $\Lambda < M_{\text{pl}}$, we can conclude that the operator of the DM decay should have a dimension larger than five. Then, we recast this condition to that for n and obtain

$$n \geq \begin{cases} 6 & \text{scalar MDM,} \\ 5 & \text{fermion MDM.} \end{cases} \quad (2.1)$$

Since we consider large $SU(2)_L$ multiplets, the RGE running of the $SU(2)_L$ gauge structure constant α_2 above the MDM mass is drastically modified. At the one-loop level, we have (see for example [40])

$$\alpha_2^{-1}(Q) = \alpha_2^{-1}(M_{\text{MDM}}) - \frac{b_2}{2\pi} \ln \frac{Q}{M_{\text{MDM}}}, \quad (2.2)$$

$$b_2 \equiv -\frac{19}{6} + c \frac{n^3 - n}{18}, \quad (2.3)$$

$SU(2)_L$	Quntum numbers		DM stability	Not excluded by direct detection	Examples
	$U(1)_Y$	Spin			
2	1/2	Scalar			
2	1/2	Fermion			Higgsino
3	0	Scalar		✓	[41]
3	0	Fermion		✓	Wino
3	1	Scalar/Fermion			[41]
4	1/2	Scalar/Fermion			[41]
4	3/2	Scalar/Fermion			[41]
5	0	Scalar		✓	[41]
5	0	Fermion	✓	✓	[37–39]
5	1	Scalar			
5	1	Fermion	✓		
5	2	Scalar			
5	2	Fermion	✓		
6	1/2, 3/2, 5/2	Scalar	✓		
7	0	Scalar	✓	✓	[37–39]
7	1, 2, 3	Scalar	✓		

Table 4: Table of the MDM properties. In the first three columns, we show the quantum numbers of our choice. In the next two columns, the DM stability (the checkmark means ”stable”) and its status under the DM direct detection experiment (the checkmark means it is still alive) are shown. The last column is devoted to the examples in the literature.

with $c = 1$ ($1/4$) for a Majorana/Weyl fermion (real scalar). Note that the first and second term of Eq. (2.3) represent the contributions from SM particles and the MDM, respectively. Then, assuming the perturbativity of $SU(2)_L$ gauge coupling upto M_{pl} , this relationship puts an upper bound on the choice of n . According to the strong dependence on n of b_2 , a strong bound is obtained,

$$n \leq \begin{cases} 8 & \text{real scalar MDM,} \\ 5 & \text{Majorana fermion MDM.} \end{cases} \quad (2.4)$$

In Table 4, we summarize the properties of MDMs for several different choices of (n, Y) . Throughout the table, the checkmark represents a suitable property as a DM candidate.

WIMP DM candidate	Quantum numbers			Masses	
	$SU(2)_L$	$U(1)_Y$	Spin	m_χ/TeV	$\Delta m_\chi/\text{MeV}$
Higgsino	2	1/2	Dirac fermion	1.1	341
Wino	3	0	Majorana fermion	2.9	166
5-plet scalar	5	0	real scalar	9.4	166
5-plet fermion	5	0	Majorana fermion	10	166

Table 5: Table of properties of WIMPs discussed in this thesis. In the “Quantum numbers” block, the $SU(2)_L$ and $U(1)_Y$ charges and spin nature are shown. In the “Masses” block, the proper mass of the thermally produced DM m_χ and mass difference between the neutral and charged components of the multiplet Δm_χ are shown. See Sec. ?? (♣ **Caution!!** ♣) for the descriptions and implications of m_χ and Sec. ?? (♣ **Caution!!** ♣) for those of Δm_χ .

In the first three columns, we show the quantum numbers of our choice, namely the set of (n, y) and spin. In the next column, we show the condition for the DM stability, namely, whether all the DM decay operators have dimensions larger than five or not. The checkmarks correspond to the automatically stable DM candidates. The next column shows if the DM direct detection experiment has already excluded these DM candidates or not. Since the non-zero value of Y usually leads to the large cross section as will be discussed in Sec. ??? (♣ **Caution!!** ♣), only $Y = 0$ candidates are associated with checkmarks. (♣ **Correct? in particular for 5- and 7-plets? References??** ♣) However, note that these properties may be changed due to a small modification to the model, such as imposition of an extra symmetry or the mixing between other new physics particles. The final column shows examples of the viable DM candidates analyzed in the literature.

From the table, we can see that there are two fascinating targets, a 5-plet fermion and a 7-plet scalar both of which has $Y = 0$. Among them, we neglect the latter possibility because it has been pointed out [42, 43] that a dimension five operator combined with a loop consisted of the TeV scale 7-plet induces a sizable decay rate for the $U(1)_{\text{EM}}$ neutral component. Instead, we will take a 5-plet scalar with $Y = 0$ just as a working example, assuming that its stability is ensured by some other mechanism.

2.3 Summary

In Table 5, we summarize the properties of WIMPs discussed in this thesis. In the first block named “Quantum numbers”, we show the $SU(2)_L$ electroweak charge, $U(1)_Y$ hypercharge, and spin nature. In the second block named “Masses”, two types of masses are shown. m_χ is the required masses to explain the DM relic abundance without non-thermal production

(see Sec. ?? **(♣ Caution!! ♣)** for the detail). Δm_χ is the mass difference between the electromagnetically neutral and charged components of the multiplet, as discussed in Sec. ?? **(♣ Caution!! ♣)**. Values are taken from [38, 41, 44–47].

Section 3

WIMP as a dark matter

3.1 WIMP dark matter relic abundance

One of the most important evidences of the beyond SM is the existence of dark matter (DM) [48]. DM is an unknown object that occupies a non-negligible ratio of the total energy of our universe, but has not yet been directly observed because of its weak interaction with the SM particles.^{‡6} In spite of its invisibility, the existence of DM is confirmed by several astrophysical observations such as the mass measurement using the gravitational lensing effect caused by galaxies and clusters [49, 50], the flatness of galactic rotation curves further the optical radius [51, 52], the measurement of the power spectrum of the cosmic microwave background (CMB), and so on. In particular, the observation of CMB allows us the precise determination of various cosmological parameters [53, 54] including the density of the non-relativistic matter and baryon, which is currently determined as [55]

$$\Omega_m h^2 = 0.1430 \pm 0.0011, \quad (3.1)$$

$$\Omega_b h^2 = 0.02237 \pm 0.00015, \quad (3.2)$$

where $h \sim \mathcal{O}(1)$ is the Hubble constant in units of $100 \text{ km s}^{-1} \text{ Mpc}^{-1}$. The difference between $\Omega_m h^2$ and $\Omega_b h^2$ implies the existence of DM and its abundance $\Omega_\chi h^2 \simeq 0.12$.

In cosmology, DM production mechanisms that try to explain the DM abundance are divided into two main categories: thermal and non-thermal production. The former assumes the equilibrium between the DM and the thermal bath in the early universe. As the universe expands, the interaction rate that maintains the thermal equilibrium becomes smaller and the DM decouples from the thermal bath at some time, which is the so-called *freezeout*. As we will see below, the resulting abundance of the DM in this scenario is mainly controlled by the temperature of the thermal bath T_f when the freezeout occurs. On the other hand, non-thermal production assumes the DM production by some processes irrespective of the thermal bath such as decay of a heavy particle. Since the thermal production scenario can be realized in relatively simple setup and WIMPs are well motivated in connection with this kind of scenario, we focus on it.

We assume the stable DM particle χ with mass m_χ can pair annihilate into SM particles with some cross section σ . When DM is in thermal equilibrium with the thermal bath of temperature T , DM velocity obeys the corresponding Boltzmann distribution. Let v be the

^{‡6}At worst DM interacts with the SM particles through the gravity, which is considerably weaker than all the other known interactions. (♣ Mention to Ema paper?? ♣)

relative velocity of annihilating DM particles and $\langle\sigma v\rangle$ be the thermal average of the product of σ and v . By using this quantity, we can write down the Boltzmann equation for the DM number density n_χ as

$$\frac{d(n_\chi a^3)}{dt} = -a^3 \langle\sigma v\rangle (n_\chi^2 - n_{\text{eq}}^2), \quad (3.3)$$

where t and a are the time coordinate and the scale factor, respectively, of the Friedmann Robertson Walker metric

$$ds^2 = -dt^2 + a(t)^2 d\mathbf{x}^2, \quad (3.4)$$

while n_{eq} denotes the number density of DM in equilibrium. When DMs are non-relativistic, its temperature dependence is given by $n_{\text{eq}} \propto T^{3/2} \exp(-m_\chi/T)$. The first term of the right handed-side of Eq. (3.3) represents the annihilation rate of DM pairs that should be proportional to n_χ^2 , while the second term describes the DM creation through the inverse process. As desired, the number density does not change in time if $n_\chi = n_{\text{eq}}$. Recalling the total entropy conservation in a comoving volume $sa^3 = (\text{const})$, it turns out to be convenient to define the ratio $Y \equiv n_\chi/s$. In fact, this modification cancels the effect of the expansion of the universe $\dot{a} > 0$ from Eq. (3.3), leading to a simpler equation

$$\frac{dY}{dt} = -s \langle\sigma v\rangle (Y^2 - Y_{\text{eq}}^2), \quad (3.5)$$

with $Y_{\text{eq}} \equiv n_{\text{eq}}/s$.

Here we assume that the freezeout occurs when the relativistic radiation dominates the total energy of the universe, which will be verified to be correct later. In this case, we can derive $a \propto T^{-1}$ from the entropy conservation with $s \propto T^3$. For the numerical calculation, we define a dimensionless parameter $x \equiv m_\chi/T$. Then we can rewrite Eq. (3.5) as

$$\frac{x}{Y_{\text{eq}}} \frac{dY}{dx} = -\frac{\Gamma}{H} \left(\frac{Y^2}{Y_{\text{eq}}^2} - 1 \right), \quad (3.6)$$

where Γ denotes the DM interaction rate defined as

$$\Gamma \equiv n_{\text{eq}} \langle\sigma v\rangle. \quad (3.7)$$

Finally, $\langle\sigma v\rangle$ is known to be expanded as [56]

$$\langle\sigma v\rangle = \langle\sigma v\rangle_s + \langle\sigma v\rangle_p x^{-1} + \cdots, \quad (3.8)$$

corresponding to the s -wave, p -wave, and so on, contributions to the cross section. When $x \gg 1$, the term with the highest power of x dominates the cross section. When the x^{-p}

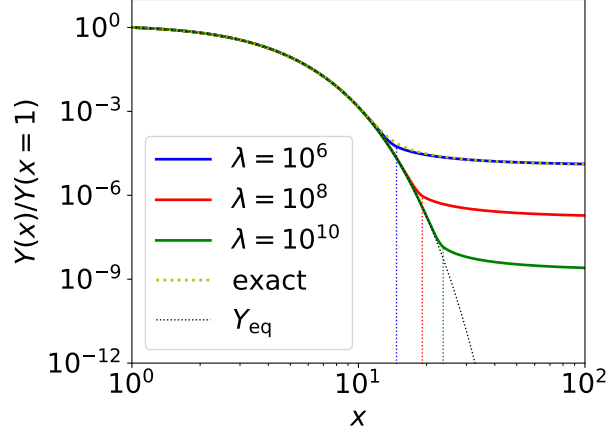


Figure 4: Plot of $Y(x)/Y(x = 1)$ with $Y(x)$ being a solution of the evolution equation Eq. (3.6). The yellow dotted line is a solution for $\lambda \equiv \Gamma/H|_{x=1} = 10^6$, while the black dotted line denotes $Y_{\text{eq}}(x)/Y_{\text{eq}}(x = 1)$. The solid lines are the approximation to the solutions described in the text. The blue, red, and green colors correspond to $\lambda = 10^8$, 10^{10} , and 10^{12} , respectively. The vertical dotted lines denote the freezeout temperature x_f .

term dominates ($p \geq 0$), temperature dependence of the interaction rate is $\Gamma \propto x^{-3/2-p}e^{-x}$, while the Hubble parameter only reduces as $H \propto \rho^{1/2} \propto x^{-2}$. As a result, at some point Γ becomes smaller than H and Y freezes out as Eq. (3.6) indicates. Hereafter, we focus on the case of the s -wave domination with $\langle \sigma v \rangle_s \neq 0$ for simplicity. **(♣ What is the difference for p -wave and so on? ♣)** In Fig. 4, we show the solution of Eq. (3.6) for $\lambda \equiv \Gamma/H|_{x=1} = 10^6$ by the yellow dotted line. In the calculation, we use the boundary condition $Y(x = 1) = Y_{\text{eq}}(x = 1)$ and plot the normalized value $Y(x)/Y(x = 1)$. We also plot the function $Y_{\text{eq}}(x)/Y_{\text{eq}}(x = 1)$ by the black dotted line.

Unfortunately, it is computationally hard to solve Eq. (3.6) for larger values of λ because of the almost complete cancellation between two terms of the right handed side for small $x \sim \mathcal{O}(1)$ and its amplification caused by large λ . We adopt instead to use an approximation that is the same with the one adopted in the public code `MicrOMEGAs` [57, 58]. For the small x region, temperature is still high enough to maintain the equilibrium $Y \simeq Y_{\text{eq}}$, which means that $d\Delta Y/dx \ll dY_{\text{eq}}/dx$ with $\Delta Y \equiv Y - Y_{\text{eq}}$. From this approximation we obtain a formula

$$\Delta Y \simeq -\frac{x}{2\lambda} \frac{dY_{\text{eq}}}{dx}. \quad (3.9)$$

Then we define the time x_f , or equivalently the so-called freezeout temperature T_f , when the approximation becomes invalid through the equation

$$\Delta Y(x_f) = 2.5Y_{\text{eq}}(x_f). \quad (3.10)$$

After the freezeout $x > x_f$, the annihilation of the DM pairs rapidly slows down and the DM abundance far exceeds its equilibrium value: $Y \gg Y_{\text{eq}}$. Then we can neglect the second term of the right hand of Eq. (3.6) and obtain the analytical solution

$$Y(x) \simeq -\frac{x}{c_1 x + \lambda/Y_{\text{eq}}(x=1)}, \quad (3.11)$$

where c_1 is a integration constant. In Fig. 4, we show results obtained with these two approximations Eqs. (3.9) and (3.11) for $\lambda = 10^6$ (blue), 10^8 (red), and 10^{10} (green). In particular, the blue and the yellow lines almost completely overlaps with each other, which proves the validity of the approximations. The vertical dotted lines in the figure show the freezeout temperature. It can be seen from the figure that $x = x_f$ does correspond to the time when Y starts to deviate from Y_{eq} . Note also that as $\lambda \propto \langle\sigma v\rangle$ becomes larger, the freezeout time becomes later and the late time relic abundance becomes smaller.

When the DM properties (*i.e.*, the mass m_χ and the annihilation cross section $\langle\sigma v\rangle$) are given, corresponding relic abundance can be calculated using above procedure. In particular, m_χ determines the normalization of the figure, namely $Y_{\text{eq}}(x=1) = Y_{\text{eq}}(T = m_\chi)$, and $\langle\sigma v\rangle$ determines the freezeout temperature through the combination of Eq. (3.7). Assuming the absence of non-thermal effect, only some good combination of these two values should explain the current relic abundance of the DM. From the numerical calculation, we obtain an order estimation formula

$$\Omega_\chi h^2 \sim \frac{3 \times 10^{-27} \text{ cm}^3/\text{s}}{\langle\sigma v\rangle_0} \sim 0.1 \left(\frac{0.01}{\alpha} \right)^2 \left(\frac{m_\chi}{300 \text{ GeV}} \right)^2, \quad (3.12)$$

where the rough estimation $\langle\sigma v\rangle \sim \alpha^2/m_\chi^2$ is used in the last equation with α being the fine structure constant for the DM-SM coupling. What is fascinating in Eq. (3.12) is that an object can be a DM candidate if it has mass comparable to the electroweak scale and coupling constant comparable to the electroweak coupling constant. This is the so-called *WIMP miracle*, which support the hypothesis of the WIMP as a candidate of the DM. Such TeV-scale WIMPs are theoretically well-motivated in connection with problems of the SM such as the naturalness problem. Several examples are briefly reviewed in the next section.

3.2 WIMP DM search : indirect detection

3.3 WIMP DM search : direct detection

3.4 Need review

(♣ Relationship between λ parameter above should be clearer ♣) WIMPs with mass around or just above the electroweak scale are theoretically well-motivated in connection with problems of the SM such as the naturalness problem. For example, the minimal

supersymmetric extension of the SM (the so-called MSSM) contains several WIMP DM candidate such as Higgsino and Wino. Another example is the minimal dark matter (MDM) model [37–39], which is a simple extension of the SM with an $SU(2)_L$ electroweak multiplet such as a 5-plet scalar / fermion. In these models, the stability of the DM is ensured by the R -parity (for the MSSM case) and by high dimensionality of the operator that describes the decay of the DM (for the MDM case). The properties of these WIMP DM candidates are summarized in Table ???. The required masses to explain the DM relic abundance through the freezeout mechanism are also shown. Since the non-relativistic annihilation cross section of TeV mass particles is significantly enhanced by the Sommerfeld enhancement effect [45, 59], there are deviations from the rough estimation formula Eq. (3.12). We will return to this point later in Sec. ??. (♣ **Caution!!** ♣) In addition, in the last column there are mass differences Δm_χ between the DM and its charged counterpart that will be explained in detail in Sec. ??. (♣ **Caution!!** ♣)

Section 4

Direct collider search of WIMPs

In this section, we review the production of TeV-scale WIMPs and search for their signals using the collider experiment. In particular, we will summarize the current bounds for WIMPs obtained at the large hadron collider (LHC) and future bounds expected at the future planned 100 TeV colliders such as the hadron option of the future circular collider (FCC-hh) [60] and the super proton-proton collider (SPPC) [61, 62]. In Sec. 4.1, we discuss the dominant production processes of WIMPs at a hadron collider. In Sec. 4.4 and (♣ ??? ♣), we review (♣ two??? ♣) different methods for the signal identification, the disappearing track search and mono-jet search (♣ ??? ♣), and summarize the current and future bounds.

4.1 WIMP production

There are two relevant processes both of which significantly contribute to the WIMP production cross section. The pair production via electroweak interaction is a universal process that can be considered for any WIMP considered in this thesis. The decay of colored particles may also be efficient particularly for the MSSM. In this subsection, we will review these two in order.

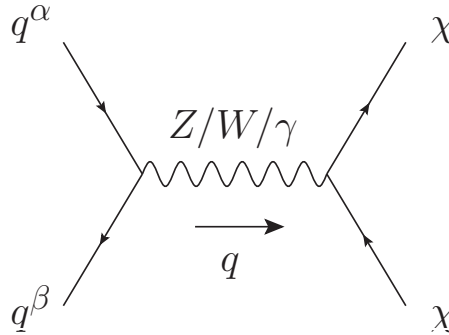


Figure 5: WIMP pair production process at the hadron collider.

Pair production via electroweak interaction

Since all the WIMPs considered here possess non-zero $SU(2)_L$ and $U(1)_Y$ charges, they can be directly produced via electroweak interaction at the hadron collider as shown in Fig. 5.^{‡7} In the figure, q^α and q^β denote the partons (namely, one of quarks or gluon) of the incident protons relevant for the process, while χ denotes the WIMP and q is the momentum transfer. Assuming the WIMP to be a $SU(2)_L$ n -plet with $U(1)_Y$ charge Y and the mass m_χ , this process is well described by the effective lagrangian^{‡8}

$$\mathcal{L} = \mathcal{L}_{\text{SM}} + (D^\mu \chi)^\dagger (D_\mu \chi) - m_\chi^2 \chi^\dagger \chi \quad (\text{complex scalar}), \quad (4.1)$$

$$\mathcal{L} = \mathcal{L}_{\text{SM}} + \bar{\chi}(i\not{D} - m_\chi)\chi \quad (\text{Dirac fermion}), \quad (4.2)$$

with \mathcal{L}_{SM} being the SM lagrangian, while the covariant derivative is given by

$$D_\mu \equiv \partial_\mu - ig_2 \mathcal{W}^a T_n^a - ig_1 Y \mathcal{B}, \quad (4.3)$$

where T_n^a ($a = 1, 2, 3$) are n -dimensional representation matrices of $SU(2)_L$. Note that when χ is a real scalar (Majorana fermion) with $Y = 0$, the terms with χ in Eq. (4.1) (Eq. (4.2)) should be divided by two.

For the calculation, we neglect the effect of the electroweak symmetry breaking, which is valid because we are interested in the high-energy collision with the parton-level center-of-mass (CM) energy $\sqrt{s'} \equiv \sqrt{q^2} \gtrsim \text{TeV}$. Then, we consider the process in the CM frame and estimate the parton-level differential cross section as

$$\left. \frac{d\sigma_{\alpha\beta}}{d\sqrt{s'}d\Omega} \right|_{\text{CM}} = \frac{C_{\alpha\beta}}{8s'} \left(1 - \frac{4m_\chi^2}{s'} \right)^{3/2} \sin^2 \theta \quad (\text{complex scalar}) \quad (4.4)$$

$$\left. \frac{d\sigma_{\alpha\beta}}{d\sqrt{s'}d\Omega} \right|_{\text{CM}} = \frac{C_{\alpha\beta}}{4s'} \sqrt{1 - \frac{4m_\chi^2}{s'}} \left[1 + \frac{4m_\chi^2}{s'} + \left(1 - \frac{4m_\chi^2}{s'} \right) \cos^2 \theta \right] \quad (\text{Dirac fermion}), \quad (4.5)$$

where θ is the angle between the momentum of the initial parton q_a and that of one of the final state WIMPs. These expressions are valid only when the center of mass energy exceeds the production threshold, $\sqrt{s'} > 2m_\chi$. Note also that these expressions represent inclusive

^{‡7}All the Feynman diagrams in this thesis are drawn with the public code **JaxoDraw-2.1** [63], which is a graphical user interface that allows users to draw Feynman diagrams intuitively and export them in the **eps** format with the help of the (modification of) **axodraw** style file for L^AT_EX [64]. Under the environment of macOS Mojave, it apparently fails to start, but one can still execute it by looking inside the application and start the Java executable file **jaxodraw-2.1-0.jar** directly. The author of this thesis would like to thank the authors for providing the best tools to write the thesis with. (♣ **Where is the first place of Feynman diagrams?** ♣)

^{‡8}In this subsection, we neglect the small mass difference among different components in the multiplet χ described in 4.4. This approximation is valid since the mass difference is by far smaller than m_χ and has only a tiny effect on the production process.

cross sections, *i.e.*, the total cross section for the production of any component of the WIMP multiplet χ . The coefficient $C_{\alpha\beta}$ consists of contributions from $U(1)_Y$ and $SU(2)_L$ gauge bosons, ^{‡9}

$$C_{\alpha\beta} = c_{1\alpha\beta} Y^2 \alpha_1^2 + c_{2\alpha\beta} I(n) \alpha_2^2, \quad (4.6)$$

with $I(n)$ being the Dynkin index for the n -dimensional representation given by

$$I(n) \equiv \frac{n^3 - n}{12}. \quad (4.7)$$

The explicit form of $c_{1\alpha\beta}$ and $c_{2\alpha\beta}$, which are sizes of the couplings between partons of our choice and gauge bosons, can be expressed using the $U(1)_Y$ charge for a parton Y_α and the $SU(2)_L$ reducible 13-dimensional representation matrices for partons $T_{\alpha\beta}^a$ as

$$c_{1\alpha\beta} = Y_\alpha^2 \delta_{\alpha\beta}, \quad (4.8)$$

$$c_{2\alpha\beta} = \sum_a |T_{\alpha\beta}^a|^2. \quad (4.9)$$

Recalling that $\alpha_1 < \alpha_2$ and that we often consider the WIMPs with large n and moderate Y , the WIMP production cross section grows as n^3 for larger multiplets according to Eq. (4.7).

As is well-known, the initial state of the hadron collider is not the individual partons but two protons. To obtain the cross section for the two protons initial state, we rely on the parton distribution function (PDF), which expresses the fraction of the partons with some given momentum in each accelerated proton. Let $f_a(x)$ ($0 < x < 1$) be the PDF for a given parton a inside a proton with momentum p^μ . $f_a(x)$ can be interpreted as a probability distribution to find the parton a with momentum xp^μ , so we have a relationship

$$\sum_a \int_0^1 dx x f_a(x) = 1, \quad (4.10)$$

associated with the total momentum conservation, and

$$\int_0^1 dx [f_d(x) - f_{\bar{d}}(x)] = 1, \quad (4.11)$$

$$\int_0^1 dx [f_u(x) - f_{\bar{u}}(x)] = 2, \quad (4.12)$$

from the composition of the proton. Using the PDF, the cross section for the process of interest at the hadron collider is evaluated as

$$\frac{d\sigma}{d\sqrt{s'} d\Omega} = \sum_{a,b} \int_0^1 dx_1 dx_2 f_a(x_1) f_b(x_2) \delta(s' - s x_1 x_2) \left. \frac{d\sigma_{ab}}{d\Omega} \right|_{\text{lab}}, \quad (4.13)$$

^{‡9}There is no contribution from the interference term between $U(1)_Y$ and $SU(2)_L$ contributions, since it is proportional to $\text{Tr}(T_n^a) = 0$.

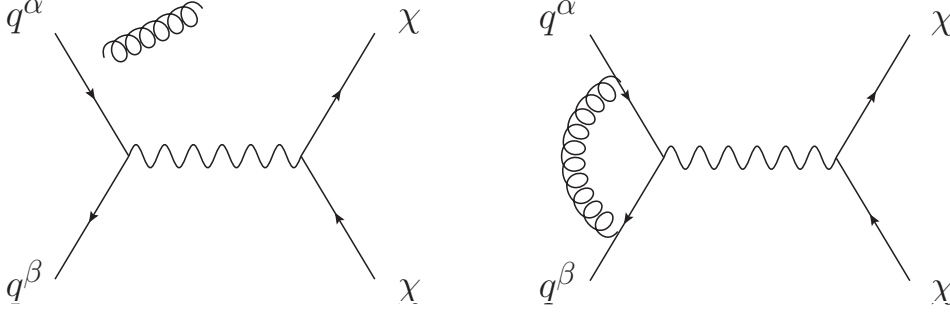


Figure 6: Example of NLO QCD contributions to the WIMP pair production process.

where \sqrt{s} is the CM energy of the proton-proton collision. Note that the cross section in the integrand is a function of x_1 and x_2 , which is obtained by performing the appropriate Lorentz transformation to $d\sigma_{ab}/d\Omega|_{\text{CM}}$. (♣ Comment on factorization scale? ♣)

Hadron colliders have several more features related to the strong interaction of quantum chromodynamics (QCD). Firstly, the next-to-leading order (NLO) QCD contribution to each process is not necessarily negligible. For the WIMP pair production, the real and virtual emission of a gluon shown in the left and right panels of Fig. 6, respectively, give the NLO QCD contributions, which will also be taken into account from now on. In particular, when the large transverse momentum is important for the phenomenology of our concern, such as the case in Sec. (♣ ??? ♣), the real emission of a gluon with sizable transverse momentum significantly modifies the calculation. Secondly, all the colored particles in the initial, intermediate, and final states should be accompanied with numbers of soft emissions of gluons, which is the phenomena so-called the parton shower. In practice, there is a difficulty caused by the partial overlap of the gluon phase space between the one-gluon emission cross section considered as an NLO QCD effect and the same considered as the parton shower. To avoid this overlap, we often perform the matching procedure, in which we set some merging energy scale by hand and include the contribution to the cross section with gluon energy above (below) the scale only from the NLO QCD (parton shower) calculation. Finally, the colored particles in the final states should eventually be confined, which is called the hadronization, and observed as some energetic and collimated sprays of hadrons, which as a whole is called jets.

In the following, we perform the numerical calculation, taking account of all the above complexities. For this purpose, we make use of the Monte Carlo generator **MadGraph5 aMC@NLO** (v2.6.3.2) [65, 66] with the successive use of **Pythia8** [67] for the parton shower, hadronization, and matching and **Delphes** (v3.4.1) [68] for the detector simulation, including the definition of jets as observed objects. We use the so-called MLM-style matching [69] with the merging scale of 67.5 GeV and **NNPDF2.3QED** with $\alpha_3(M_Z) = 0.118$ [70] as a canonical set of PDFs.

WIMP name	Higgsino	Wino	5-plet Majorana fermion	5-plet real scalar
σ_{LO} [fb]	15	52	(♣ ??? ♣)	(♣ ??? ♣)
σ_{NLO} [fb]	17	60	(♣ ??? ♣)	(♣ ??? ♣)
K -factor	1.15	1.15		

Table 6: Table of pair production cross sections of several types of WIMPs. The CM energy $\sqrt{s} = 100$ TeV is assumed and WIMP masses are set to be 1 TeV.

Wino mass [TeV]	1.0	1.5	2.0	2.9
σ_{LO} [fb]	52	12	4.0	0.86
σ_{NLO} [fb]	60	15	4.7	1.0
K -factor	1.15	1.20	1.19	1.21

Table 7: Table of pair production cross sections of Wino with several choice of masses. The CM energy $\sqrt{s} = 100$ TeV is assumed.

In Table 6, we list the production cross sections of various WIMPs via a weak gauge boson exchange at a $\sqrt{s} = 100$ TeV hadron collider. As for the WIMP mass, we use the common value $m = 1$ TeV to compare the cross sections among different choice of quantum numbers. σ_{LO} and σ_{NLO} denote the production cross sections without and with the NLO QCD correction, respectively, while the last line is the so-called K -factor defined as $K = \sigma_{\text{NLO}}/\sigma_{\text{LO}}$. From the table, by paying attention to the factor two difference in degrees of freedom between the Dirac (Higgsino) and Majorana (Wino and 5-plet) fermions, we can roughly see the dependence of the cross section on the $SU(2)_L$ charge $\sigma \propto n^3$. (♣ **Correct? Seems that Higgsino cross section is too small? ♣**)

In Table 7, we also show the mass dependence of the Wino pair production cross section. For heavier mass, wider range of $\sqrt{s'}$ is below the production threshold $2m_\chi$ or accompanied with a small suppression factor $(1 - 4m_\chi^2/s')^{1/2}$ as shown in Eq. (4.5), and the cross section becomes significantly smaller. However, values in the tables still denote that plenty of well-motivated WIMP DM candidates, such as 1 TeV Higgsino and 3 TeV Wino, are produced at, for example, the 3 ab^{-1} option of the FCC-hh.

(♣ **Histogram of $\sqrt{s'}$ ♣**)

(♣ **Histogram of angular dependence ♣**)

(♣ **Is angular dependence affected by the Lorentz boost? ♣**)

gluino mass [TeV]	6.0	7.0	8.0
$\sigma(pp \rightarrow \tilde{g}\tilde{g})$ [fb]	7.9	2.7	1.0

Table 8: Gluino pair production cross section at $\sqrt{s} = 100$ TeV.

Decay of colored particles

In hadron colliders, particles with color charges have far more chance to be produced than non-colored particles. When we consider the split SUSY or the anomaly mediation model reviewed in Sec. 2.1, gluino tends to be relatively light, whose decay produces WIMPs. Without fine-tuning of Higgsino and gaugino masses, gluino lifetime is sufficiently short and only its decay products are observed by the detectors. Since all the SUSY particles finally decay into the LSP as described in Sec. 2.1, the gluino production cross section can effectively be counted as the production cross section of WIMPs in these models.

Keeping the R-parity conservation in our mind, the dominant process accompanied with gluinos in these models is the gluino pair production. In Table 8, we summarize the gluino pair production cross section for various gluino masses at $\sqrt{s} = 100$ TeV, taken from [71]. The calculation is again performed using `MadGraph5_aMC@NLO` and only the LO QCD processes are considered. The values in the table show that the gluino pair production process, depending on its mass, may give much larger cross section for the WIMP production than the purely electroweak processes described above.

(♣ Comment on AMSB $m_{3/2}$ and L for the table? ♣)

4.2 Disappearing track search

Mass splitting among an $SU(2)_L$ multiplet

So far we have neglected the effect from the electroweak symmetry breaking and treated every component of an $SU(2)_L$ multiplet equally. However, in the reality, spontaneously breaking of the $SU(2)_L$ symmetry occurs and this results in the mass splitting among an $SU(2)_L$ multiplet as we will see from now on.

First, we consider the mass splitting caused by the tree-level propagation of heavy particles, such as the SUSY particles other than the LSP, or another unknown particles. After integrating out all the heavy particles other than the SM particles and the light WIMP, we may obtain operators of the form of $\mathcal{O} = M_{ij}\chi_i\chi_j$, where χ denotes the WIMP and i is the $SU(2)_L$ index. This operator causes the mass splitting only when M_{ij} transforms non-trivially under the $SU(2)_L$ symmetry. Then, we can explicitly construct the lowest

dimensional operator among those relevant for the mass splitting. For Higgsino,

$$\mathcal{O} = \frac{1}{\Lambda} (\bar{\chi} \Phi^*) (\Phi \chi), \quad (4.1)$$

where $\chi = (\tilde{H}_u, -i\sigma_2 \tilde{H}_d^*)^t$, Φ is the SM Higgs doublet with $Y = 1/2$, and Λ is the cut-off scale of the effective theory, *i.e.*, the typical mass scale of the relevant heavy particles.

(♣ Histogram of surviving probability ♣)

(♣ Histogram of beta distribution before / after 10cm cut ♣)

4.3 Soft lepton search

(♣ If possible ♣)

4.4 Mono-jet search

Section 5

Probing EWIMPs with Drell-Yan process at 100 TeV colliders

5.1 EWIMP effect on the lepton production processes

We investigate contributions of the EWIMPs to the Drell-Yan process through the vacuum polarization of the electroweak gauge bosons at the loop level. Throughout the paper, we assume that all the other beyond the SM particles are heavy enough so that they do not affect the following discussion. After integrating out the EWIMPs, the effective lagrangian is expressed as

$$\mathcal{L}_{\text{eff}} = \mathcal{L}_{\text{SM}} + C_2 g^2 W_{\mu\nu}^a f\left(-\frac{D^2}{m^2}\right) W^{a\mu\nu} + C_1 g'^2 B_{\mu\nu} f\left(-\frac{\partial^2}{m^2}\right) B^{\mu\nu}, \quad (5.1)$$

where \mathcal{L}_{SM} is the SM Lagrangian, D is a covariant derivative, m is the EWIMP mass,^{‡10} g and g' are the $SU(2)_L$ and $U(1)_Y$ gauge coupling constants, and $W_{\mu\nu}^a$ and $B_{\mu\nu}$ are the field strength associated with the $SU(2)_L$ and $U(1)_Y$ gauge group, respectively. The function $f(x)$ is defined as^{‡11}

$$f(x) = \begin{cases} \frac{1}{16\pi^2} \int_0^1 dy y(1-y) \ln(1-y(1-y)x - i0) & \text{(Fermion),} \\ \frac{1}{16\pi^2} \int_0^1 dy (1-2y)^2 \ln(1-y(1-y)x - i0) & \text{(Scalar),} \end{cases} \quad (5.2)$$

where the first (second) line corresponds to a fermionic (scalar) EWIMP, respectively. The coefficients C_1 and C_2 for an $SU(2)_L$ n -plet EWIMP with hypercharge Y are given by

$$C_1 = \frac{\kappa}{8} n Y^2, \quad (5.3)$$

$$C_2 = \frac{\kappa}{8} I(n), \quad (5.4)$$

where $\kappa = 1, 2, 8, 16$ for a real scalar, a complex scalar, a Weyl or Majorana fermion, and a Dirac fermion, respectively. The Dynkin index $I(n)$ for the n dimensional representation of

^{‡10}Here we neglect a small mass splitting among the $SU(2)_L$ multiplet.

^{‡11}If an EWIMP interacts only through the electroweak interaction, its decay width is of $O(1)\%$ or less of its mass even if it is unstable. We assume that this is the case, and neglect the small effect on the function $f(x)$ due to the small decay width.

Fermion f	$v_f^{(\gamma)}$	$a_f^{(\gamma)}$	$v_f^{(Z)}$	$a_f^{(Z)}$	$v_f^{(W)}$	$a_f^{(W)}$
up-type quark	$\frac{2}{3}e$	0	$(\frac{1}{4} - \frac{2}{3}s_W^2)g_Z$	$-\frac{1}{4}g_Z$	$\frac{1}{2\sqrt{2}}g$	$-\frac{1}{2\sqrt{2}}g$
down-type quark	$-\frac{1}{3}e$	0	$(-\frac{1}{4} + \frac{1}{3}s_W^2)g_Z$	$\frac{1}{4}g_Z$	$\frac{1}{2\sqrt{2}}g$	$-\frac{1}{2\sqrt{2}}g$
lepton	$-e$	0	$(-\frac{1}{4} + s_W^2)g_Z$	$\frac{1}{4}g_Z$	$\frac{1}{2\sqrt{2}}g$	$-\frac{1}{2\sqrt{2}}g$

Table 9: Coefficients of the weak interaction defined as $\Gamma_f^{(V)} \equiv v_f^{(V)} + a_f^{(V)}\gamma_5$. Here, $e = g_{SW}$ and $g_Z = g/c_W$, where $s_W \equiv \sin \theta_W$ and $c_W \equiv \cos \theta_W$ with θ_W being the weak mixing angle.

$SU(2)_L$ is given by

$$I(n) = \frac{1}{12}(n^3 - n), \quad (5.5)$$

which is normalized so that $I(2) = 1/2$. The coefficients are uniquely determined by the representation of the EWIMPs. For example, $(C_1, C_2) = (1, 1)$ for Higgsino, and $(C_1, C_2) = (0, 2)$ for Wino. We emphasize that, contrary to the usual effective field theory, our prescription is equally applied when the typical scale of the gauge boson four-momentum, q , is larger than the EWIMP mass scale m since we do not perform a derivative expansion of f in Eq. (5.1). It is important because, as we see soon, the effect of the EWIMPs are maximized when $\sqrt{q^2} \sim m$, where the derivative expansion is not applicable.

At the leading order (LO), we are interested in $u(p) \bar{u}(p') \rightarrow \ell^-(k) \ell^+(k')$ and $d(p) \bar{d}(p') \rightarrow \ell^-(k) \ell^+(k')$ as the NC processes and $u(p) \bar{d}(p') \rightarrow \nu(k) \ell^+(k')$ and $d(p) \bar{u}(p') \rightarrow \ell^-(k) \bar{\nu}(k')$ as the CC processes. Here, u and d collectively denote up-type and down-type quarks, respectively, and p, p', k , and k' are initial and final state momenta. In the SM, the amplitudes for both the NC and CC processes at the LO are expressed as

$$\mathcal{M}_{\text{SM}} = \sum_V \frac{[\bar{v}(p')\gamma^\mu \Gamma_q^{(V)} u(p)] [\bar{u}(k)\gamma_\mu \Gamma_\ell^{(V)} v(k')]}{s' - m_V^2}, \quad (5.6)$$

where $\sqrt{s'}$ is the invariant mass of the final state leptons, which is denoted as $m_{\ell\ell}$ for the NC processes and $m_{\ell\nu}$ for the CC processes. The relevant gauge bosons are $V = \gamma, Z$ for the NC processes and $V = W^\pm$ for the CC processes, with m_V being the corresponding gauge boson mass. In addition,

$$\Gamma_f^{(V)} \equiv v_f^{(V)} + a_f^{(V)}\gamma_5, \quad (5.7)$$

with $v_f^{(V)}$ and $a_f^{(V)}$ given in Tab. 9. The EWIMP contribution is given by

$$\mathcal{M}_{\text{EWIMP}} = \sum_{V, V'} C_{VV'} s' f \left(\frac{s'}{m^2} \right) \frac{[\bar{v}(p')\gamma^\mu \Gamma_q^{(V)} u(p)] [\bar{u}(k)\gamma_\mu \Gamma_\ell^{(V')} v(k')]}{(s' - m_V^2)(s' - m_{V'}^2)}, \quad (5.8)$$

where $C_{\gamma\gamma} = 4(C_1 g'^2 c_W^2 + C_2 g^2 s_W^2)$, $C_{\gamma Z} = C_{Z\gamma} = 4(C_2 g^2 - C_1 g'^2) s_W c_W$, $C_{ZZ} = 4(C_1 g'^2 s_W^2 + C_2 g^2 c_W^2)$, and $C_{WW} = 4C_2 g^2$. Again $V, V' = \gamma, Z$ for the NC processes and $V, V' = W^\pm$ for the CC processes.

We use $d\Pi_{\text{LIPS}}$ for a Lorentz invariant phase space factor for the two particles final state. Then, using Eqs. (5.6) and (5.8), we define

$$\frac{d\sigma_{\text{SM}}}{d\sqrt{s'}} = \sum_{a,b} \frac{dL_{ab}}{d\sqrt{s'}} \int d\Pi_{\text{LIPS}} |\mathcal{M}_{\text{SM}}(q_a \bar{q}_b \rightarrow \ell\ell/\ell\nu)|^2, \quad (5.9)$$

$$\frac{d\sigma_{\text{EWIMP}}}{d\sqrt{s'}} = \sum_{a,b} \frac{dL_{ab}}{d\sqrt{s'}} \int d\Pi_{\text{LIPS}} 2\Re[\mathcal{M}_{\text{SM}}\mathcal{M}_{\text{EWIMP}}^*(q_a \bar{q}_b \rightarrow \ell\ell/\ell\nu)], \quad (5.10)$$

where we take the average and summation over spins. Here, $dL_{ab}/d\sqrt{s'}$ is the luminosity function for a fixed $\sqrt{s'}$:

$$\frac{dL_{ab}}{d\sqrt{s'}} \equiv \frac{1}{s} \int_0^1 dx_1 dx_2 f_a(x_1) f_b(x_2) \delta\left(\frac{s'}{s} - x_1 x_2\right), \quad (5.11)$$

where a and b denote species of initial partons, \sqrt{s} is the center of mass energy of the proton collision ($\sqrt{s} = 100$ TeV in our case), and $f_a(x)$ is a parton distribution function (PDF) of the given parton a . Eq. (5.9) represents the SM cross section, while Eq. (5.10) the EWIMP contribution to the cross section. For the statistical treatment in the next section, we introduce a parameter μ that parametrizes the strength of the EWIMP effect, and express the cross section with μ as

$$\frac{d\tilde{\sigma}}{d\sqrt{s'}} = \frac{d\sigma_{\text{SM}}}{d\sqrt{s'}} + \mu \frac{d\sigma_{\text{EWIMP}}}{d\sqrt{s'}}. \quad (5.12)$$

Obviously, $\mu = 0$ corresponds to the pure SM, while $\mu = 1$ corresponds to the SM+EWIMP model. Hereafter, we use

$$\delta_\sigma(\sqrt{s'}) \equiv \frac{d\sigma_{\text{EWIMP}}/d\sqrt{s'}}{d\sigma_{\text{SM}}/d\sqrt{s'}}, \quad (5.13)$$

to denote the correction from the EWIMP.

In Fig. 7, we plot δ_σ for the CC processes as a function of $\sqrt{s'}$. The purple, blue, and red lines correspond to Higgsino, Wino, and 5-plet scalar, respectively. There is a dip around $\sqrt{s'} = 2m$ for all the cases of the EWIMPs which originates from the loop function f in Eq. (5.2). The EWIMP contributions to the NC processes show a similar dip structure that again comes from f . This dip is crucial not only for the discovery of the EWIMP signal (see Sec. 5.2.3) but also for the determination of the properties of the EWIMPs (see Sec. 5.2.4). In particular, the EWIMP mass can be extracted from the dip position, while the EWIMP charges (n and Y) can be determined from the depth of the dip.

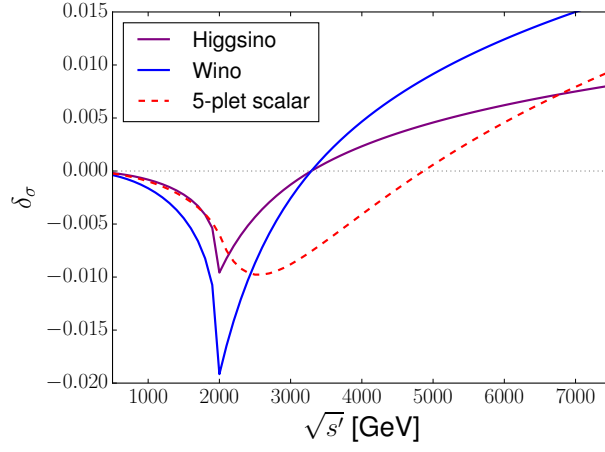


Figure 7: δ_σ for the CC processes as a function of $\sqrt{s'} = m_{\ell\nu}$. The purple, blue, and red lines correspond to Higgsino, Wino, and 5-plet real scalar, respectively.

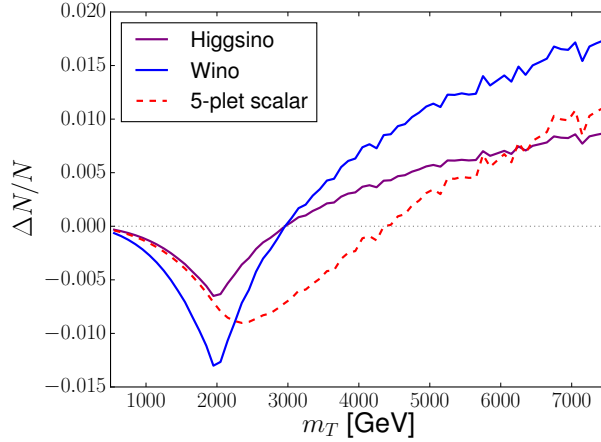


Figure 8: The EWIMP effect on the ratio of the number of events $\Delta N/N$ as a function of m_T . The line colors are the same as Fig. 7.

For the NC processes, the momenta of two final state charged leptons are measurable and we can use the invariant mass distribution of the number of events for the study of the EWIMPs. For the CC processes, on the contrary, we cannot measure the momentum of the neutrino in real experiments, and hence we instead use the missing transverse momentum $p_{T,\text{miss}}$. We use the transverse mass defined as

$$m_T^2 \equiv 2p_{T,\ell} p_{T,\text{miss}} (1 - \cos(\phi_{T,\ell,\text{miss}})) , \quad (5.14)$$

where $p_{T,\ell}$ denotes the transverse momentum of the charged lepton and $\phi_{T,\ell,\text{miss}} \equiv \phi_\ell - \phi_{\text{miss}}$ is the difference between the azimuth angles of $p_{T,\ell}$ and $p_{T,\text{miss}}$. The important property

of m_T is that the distribution of m_T peaks at $m_T = m_{\ell\nu}$. Because of this property, the characteristic shape of δ_σ remains in the m_T distribution in the CC events. To see this, we plot in Fig. 8 the EWIMP effect on the number of events as a function of m_T . Here, the vertical axis is the ratio of the EWIMP correction to the number of events ΔN to the number of events in the SM N for each bin with the bin width of 100 GeV.^{‡12} We find that the dip structure remains in the m_T distribution, though the depth of the dip is smaller compared to the $m_{\ell\nu}$ distribution.

5.2 Analysis

5.2.1 Event generation

Now we discuss how well we can extract information about EWIMPs from the invariant mass and transverse mass distributions for the processes of our concern at future 100 TeV pp collider experiments. We take into account the effects of the next-to-leading order QCD corrections in the events as well as detector effects through Monte-Carlo simulations.

In our analysis, we first generate the SM event sets for the NC processes $pp \rightarrow e^-e^+/\mu^-\mu^+$ and for the CC processes $pp \rightarrow e^\pm\nu_e/\mu^\pm\nu_\mu$. We use `MadGraph5_aMC@NLO` (v2.6.3.2) [65, 66] for the event generation with the successive use of `Pythia8` [67] for the parton shower and the hadronization and `Delphes` (v3.4.1) [68] with the card `FCChh.tcl` for the detector simulation. We use `NNPDF2.3QED` with $\alpha_s(M_Z) = 0.118$ [70] as a canonical set of PDFs. For the renormalization and factorization scales, we use the default values of `MadGraph5_aMC@NLO`, i.e., the central m_T^2 scale after k_T -clustering of the event (which we denote by Q). The events are binned by the characteristic mass m_{char} for each process: we use the lepton invariant mass $m_{\text{char}} = m_{\ell\ell}$ for the NC processes, and the transverse mass $m_{\text{char}} = m_T$ for the CC processes, respectively. In both cases, we generated events with the characteristic mass within the range of $500 \text{ GeV} < m_{\text{char}} < 7.5 \text{ TeV}$ and divide them into 70 bins with the equal width of 100 GeV.

As for the event selection by a trigger, we may have to impose some cut on the lepton transverse momentum p_T . As we will see, we concentrate on events with high p_T charged lepton(s) with which we expect the event may be triggered. For the NC processes, we use events with at least two high p_T leptons. For our analysis, we use events with $m_{\ell\ell} > 500 \text{ GeV}$; we assume that such events are triggered by using two energetic charged leptons so that we do not impose extra kinematical requirements. On the contrary, the CC events are characterized only by a lepton and a missing transverse momentum. For such events, we require that the

^{‡12}Just for an illustrative purpose, we generate events corresponding to the integrated luminosity $\mathcal{L} = 1 \text{ ab}^{-1}$ for this figure, which is not the same luminosity as we use in the next section (see Sec. 5.2.1 for details of the event generation).

p_T of the charged lepton should be larger than 500 GeV.^{‡13} For the CC events, the cut reduces the number of events in particular for the bins with the low transverse mass $m_T \sim 500$ GeV, and thus affects the sensitivity of the CC processes to relatively light EWIMPs. We will come back to this point later.

The EWIMP effect is incorporated by rescaling the SM event by δ_σ defined in Eq. (5.13). With the parameter μ defined in Eq. (5.12), the number of events corresponding to the SM+EWIMP hypothesis in i -th bin, characterized by $m_{i,\min} < m_{\text{char}} < m_{i,\max}$, is

$$x_{f,i}(\mu) = \sum_{m_{i,\min} < m_{\text{char}} < m_{i,\max}} \left[1 + \mu \delta_\sigma(\sqrt{s'}) \right], \quad (5.1)$$

where the sum runs over all the events of the final state f whose characteristic mass m_{char} (after taking into account the detector effects) falls into the bin. Note that the true value of $\sqrt{s'}$ should be used for each event for the computation of δ_σ : we extract it from the hard process information.^{‡14}

5.2.2 Statistical treatment

We now explain the statistical method we will adopt in our analysis. We collectively denote our theoretical model as $\mathbf{x}_f(\mu) = \{x_{f,i}(\mu)\}$, where $x_{f,i}(\mu)$ is given by Eq. (5.1). We denote the experimental data set as $\tilde{\mathbf{x}}_f$ that in principle is completely unrelated to our theoretical model $\mathbf{x}_f(\mu)$. Since we do not have an actual experimental data set for 100 TeV colliders for now, however, we take $\tilde{\mathbf{x}}_f = \mathbf{x}_f(\mu = 1)$ (for some fixed values of the EWIMP mass and charges) throughout our analysis, assuming that the EWIMP does exist. In particular, this choice tests the SM-only hypothesis if we take our theoretical model as $\mathbf{x}_f(\mu = 0)$.

If the expectation values of $x_{f,i}(\mu)$ are precisely known, the sensitivity to EWIMPs can be studied only with statistical errors. In reality, however, the computation of $x_{f,i}(\mu)$ suffers various sources of uncertainties, which results in systematic errors in our theoretical model. The sources include errors in the integrated luminosity, the beam energy, choices of the renormalization and the factorization scales, choices of PDF, the pile-up effect, higher order corrections to the cross section, and so on. In order to deal with these uncertainties, we introduce sets of free parameters $\boldsymbol{\theta}_f = \{\theta_{f,\alpha}\}$ (i.e. nuisance parameters) which absorb (smooth) uncertainties of the number of events, and modify our theoretical model as

$$\tilde{x}_{f,i}(\boldsymbol{\theta}_f, \mu) \equiv x_{f,i}(\mu) f_{\text{sys},i}(\boldsymbol{\theta}_f), \quad (5.2)$$

^{‡13}In the ATLAS analysis of the mono-lepton signal during the 2015 (2016) data taking period [72], they use the event selection condition $p_T > 24$ (60) GeV for leptons that satisfy the *medium* identification criteria. In the CMS analysis during the period on 2016 [73], they use the condition $p_T > 130$ (53) GeV for an electron (a muon).

^{‡14}The p_T cut for the CC process does not affect this estimation since the EWIMP does not modify the angular distribution of the final lepton and neutrino for the CC process.

where $f_{\text{sys},i}(\boldsymbol{\theta}_f)$ is a function that satisfies $f_{\text{sys},i}(\mathbf{0}) = 1$. We expect that, if the function $f_{\text{sys},i}$ is properly chosen, the true distribution of the number of events in the SM is given by $\tilde{\mathbf{x}}_f(\boldsymbol{\theta}_f, 0) = \{\tilde{x}_{f,i}(0)f_{\text{sys},i}(\boldsymbol{\theta}_f)\}$ for some value of $\boldsymbol{\theta}_f$. In our analysis, we adopt the five parameters fitting function given by [74]

$$f_{\text{sys},i}(\boldsymbol{\theta}_f) = e^{\theta_{f,1}}(1 - p_i)^{\theta_{f,2}}p_i^{(\theta_{f,3} + \theta_{f,4} \ln p_i + \theta_{f,5} \ln^2 p_i)}, \quad (5.3)$$

where $p_i = 2m_i/\sqrt{s}$ with m_i being the central value of the lepton invariant mass (transverse mass) of the i -th bin for the NC (CC) processes. As we will see, the major effects of systematic errors can be absorbed into $\boldsymbol{\theta}_f$ with this fitting function.

In order to test the SM-only hypothesis, we define the following test statistic [75]:

$$q_0 \equiv -2 \sum_{f=\ell\ell, \ell\nu} \ln \frac{L(\tilde{\mathbf{x}}_f; \hat{\boldsymbol{\theta}}_f, \mu = 0)}{L(\tilde{\mathbf{x}}_f; \hat{\boldsymbol{\theta}}_f, \hat{\mu})}. \quad (5.4)$$

Here, $\hat{\boldsymbol{\theta}}_f$ and $\{\hat{\boldsymbol{\theta}}_f, \hat{\mu}\}$ are determined so that $\prod_f L(\tilde{\mathbf{x}}_f; \boldsymbol{\theta}_f, \mu = 0)$ and $\prod_f L(\tilde{\mathbf{x}}_f; \boldsymbol{\theta}_f, \mu)$ are maximized, respectively. The likelihood function is defined as

$$L(\tilde{\mathbf{x}}_f; \boldsymbol{\theta}_f, \mu) \equiv L_{\boldsymbol{\theta}_f}(\tilde{\mathbf{x}}_f; \mu) L'(\boldsymbol{\theta}_f; \boldsymbol{\sigma}_f), \quad (5.5)$$

where

$$L_{\boldsymbol{\theta}_f}(\tilde{\mathbf{x}}_f; \mu) \equiv \prod_i \exp \left[-\frac{(\tilde{x}_{f,i} - \tilde{x}_{f,i}(\boldsymbol{\theta}_f, \mu))^2}{2\tilde{x}_{f,i}(\boldsymbol{\theta}_f, \mu)} \right], \quad (5.6)$$

$$L'(\boldsymbol{\theta}_f; \boldsymbol{\sigma}_f) \equiv \prod_{\alpha} \exp \left[-\frac{\theta_{f,\alpha}^2}{2\sigma_{f,\alpha}^2} \right]. \quad (5.7)$$

The product in Eq. (5.6) runs over all the bins, while the product in Eq. (5.7) runs over all the free parameters we introduced. For each $\theta_{f,\alpha}$, we define the “standard deviation” $\sigma_{f,\alpha}$, which parametrizes the possible size of $\theta_{f,\alpha}$ within the SM with the systematic errors.^{‡15} If the systematic errors are negligible compared with the statistical error, we can take $\boldsymbol{\sigma}_f \rightarrow \mathbf{0}$, while the analysis with $\boldsymbol{\sigma}_f \rightarrow \infty$ assumes no knowledge of systematic errors and gives a conservative result. We identify $(q_0)^{1/2} = 5$ (1.96) as the detection reach at the 5σ (95% C.L.) level, since q_0 asymptotically obeys a chi-square distribution with the degree of freedom one.

In order to determine $\boldsymbol{\sigma}_f$, we consider the following sources of the systematic errors:

- Luminosity ($\pm 5\%$ uncertainty is assumed),

^{‡15}Here we assume the Gaussian form for the nuisance parameter distribution. The dependence of the results on the choice of the distribution will be discussed later in Sec. 5.2.3.

- Renormalization scale ($2Q$ and $Q/2$, instead of Q),
- Factorization scale ($2Q$ and $Q/2$, instead of Q),
- PDF choice (We use 101 variants of NNPDF2.3QED with $\alpha_s(M_Z) = 0.118$ [70] provided by LHAPDF6 [76] with IDs ranging from 244600 to 244700).

The values of σ_f are determined as follows. Let \mathbf{y}_f be the set of number of events in the SM for the final state f with the canonical choices of the parameters, and \mathbf{y}'_f be that with one of the sources of the systematic errors being varied. We minimize the chi-square function defined as

$$\chi_f^2 \equiv \sum_i \frac{(y'_{f,i} - \tilde{y}_{f,i}(\boldsymbol{\theta}_f))^2}{\tilde{y}_{f,i}(\boldsymbol{\theta}_f)}, \quad (5.8)$$

where

$$\tilde{y}_{f,i}(\boldsymbol{\theta}_f) \equiv y_{f,i} f_{\text{sys},i}(\boldsymbol{\theta}_f), \quad (5.9)$$

for each final state f , and determine the best-fit values of $\boldsymbol{\theta}_f$ for each set of \mathbf{y}'_f . We repeat this process for different sets of \mathbf{y}'_f , and σ_f are determined from the distributions of the best-fit values of $\boldsymbol{\theta}_f$. For example, let us denote the best-fit values for the fit associated with the luminosity errors $\pm 5\%$ as $\boldsymbol{\theta}_f^\pm$. We estimate σ_f associated with these errors, denoted here as $\sigma_f^{\text{lumi.}}$, as

$$\sigma_{f,\alpha}^{\text{lumi.}} = \sqrt{\frac{(\theta_{f,\alpha}^+)^2 + (\theta_{f,\alpha}^-)^2}{N}}, \quad (5.10)$$

where N denotes the number of fitting procedures we have performed: $N = 2$ for this case. We estimate σ_f associated with the other sources of the errors, denoted as $\sigma_f^{\text{ren.}}$, $\sigma_f^{\text{fac.}}$, and σ_f^{PDF} , in a similar manner. Finally, the total values of σ_f are obtained by combining all the sources together as^{‡16}

$$\sigma_{f,\alpha} = \sqrt{(\sigma_{f,\alpha}^{\text{lumi.}})^2 + (\sigma_{f,\alpha}^{\text{ren.}})^2 + (\sigma_{f,\alpha}^{\text{fac.}})^2 + (\sigma_{f,\alpha}^{\text{PDF}})^2}. \quad (5.11)$$

In Tables 10 and 11, we show the values of σ_{ee} and $\sigma_{e\nu_e}$ associated with each source of the systematic errors, respectively. These values can be interpreted as the possible size of the fit parameters within the SM, which is caused by the systematic uncertainties. As explained in Eq. (5.11), we combine these values in each column to obtain σ_f . In Table 12,

^{‡16}There may be some correlations between the distribution of nuisance parameters $\boldsymbol{\theta}_f$. In this paper, we treat each of them as obeying to an independent Gaussian distribution for simplicity.

Sources of systematic errors	$\sigma_{ee,1}$	$\sigma_{ee,2}$	$\sigma_{ee,3}$	$\sigma_{ee,4}$	$\sigma_{ee,5}$
Luminosity: $\pm 5\%$ ($\sigma_{ee}^{\text{lumi.}}$)	0.05	0	0	0	0
Renormalization scale: $2Q, Q/2$ ($\sigma_{ee}^{\text{ren.}}$)	0.4	0.6	0.3	0.05	0.004
Factorization scale: $2Q, Q/2$ ($\sigma_{ee}^{\text{fac.}}$)	0.3	0.5	0.2	0.06	0.004
PDF choice (σ_{ee}^{PDF})	0.4	0.7	0.3	0.06	0.004

Table 10: Values of σ_{ee} for each source of systematic errors. The result is the same for the $\mu\mu$ final state.

Sources of systematic errors	$\sigma_{e\nu_e,1}$	$\sigma_{e\nu_e,2}$	$\sigma_{e\nu_e,3}$	$\sigma_{e\nu_e,4}$	$\sigma_{e\nu_e,5}$
Luminosity: $\pm 5\%$ ($\sigma_{e\nu_e}^{\text{lumi.}}$)	0.05	0	0	0	0
Renormalization scale: $2Q, Q/2$ ($\sigma_{e\nu_e}^{\text{ren.}}$)	0.3	0.4	0.2	0.04	0.003
Factorization scale: $2Q, Q/2$ ($\sigma_{e\nu_e}^{\text{fac.}}$)	1.0	1.6	0.6	0.1	0.01
PDF choice ($\sigma_{e\nu_e}^{\text{PDF}}$)	0.6	0.9	0.4	0.08	0.006

Table 11: Best fit values of fit parameters for several sources of systematic errors for the $e\nu_e$ final state. The result is the same for the $\mu\nu_\mu$ final state.

we summarize the result of the combination for all the final states. The values of σ_f are independent of the final state lepton flavors since the energy scale of our concern is much higher than the lepton masses. However, we use different sets of fit parameters θ_{ee} and $\theta_{\mu\mu}$ for the NC processes and $\theta_{e\nu_e}$ and $\theta_{\mu\nu_\mu}$ for the CC processes because of the different detector response to electrons and muons.

In the tables, we have neglected the systematic errors from the detector effect. The main errors are expected to come from the lepton identification, in which some of the leptons in any process are overlooked or identified incorrectly, resulting in the misreconstruction of the event topology. Since we perform the fitting procedure as Eq. (5.4), it is expected that the small and smooth modification of the number of events as a function of the lepton invariant mass may be absorbed into the choice of nuisance parameters, if the corresponding values of σ_f are properly taken into account in addition to the values in Table 10. What is dangerous is the possible jerky modification that mimics the EWIMP signal, which may be induced by the detector setup, the complicated detector response to leptons, and so on. In this paper, we just assume that these systematic errors from the detector effect are well controlled once the real experiment will start and focus on the theoretical uncertainties listed in tables.

Final state f	$\sigma_{f,1}$	$\sigma_{f,2}$	$\sigma_{f,3}$	$\sigma_{f,4}$	$\sigma_{f,5}$
ee	0.7	1.0	0.4	0.09	0.008
$\mu\mu$	0.7	1.0	0.4	0.09	0.008
$e\nu_e$	1.2	1.9	0.7	0.2	0.01
$\mu\nu_\mu$	1.2	1.9	0.7	0.2	0.01

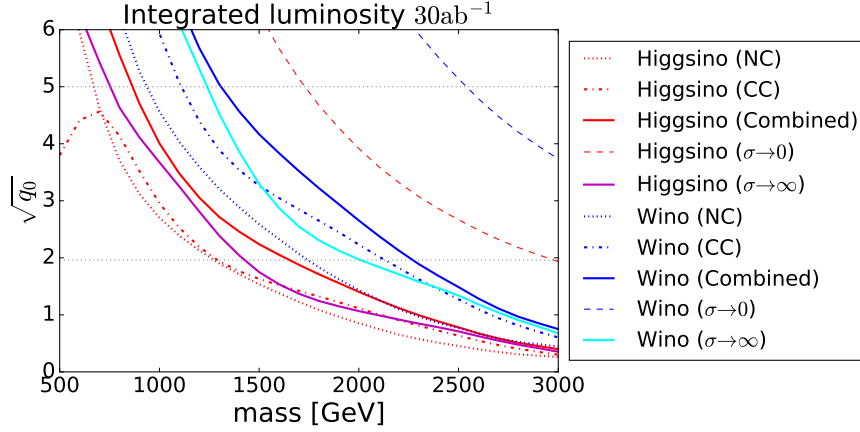
Table 12: Summary of standard deviations σ_f for each final state.

Figure 9: $\sqrt{q_0}$ as a function of the EWIMP mass. Red and blue lines correspond to the Higgsino and Wino, respectively, while line styles represent the result from the NC processes, the CC processes, the combined analysis, and the combined analysis with the optimistic $\sigma_f \rightarrow 0$ limit. The purple and cyan lines correspond to the results from the conservative analysis with $\sigma_f \rightarrow \infty$ for the Higgsino and Wino, respectively.

5.2.3 Detection reach

Now we show the detection reach of EWIMPs at future 100 TeV colliders. In Fig. 9, we plot the value of $\sqrt{q_0}$ as a function of the EWIMP mass, with the integrated luminosity $\mathcal{L} = 30 \text{ ab}^{-1}$. As representative scenarios, we show the cases for Higgsino (the red lines) and Wino (the blue lines). The dotted and dash-dotted lines are the result obtained only from the NC processes and the CC processes, respectively. We find that the CC processes are more sensitive to the effect of the EWIMPs than the NC processes because of the larger cross section. This result is consistent with Refs. [77, 78]. The sensitivity of the CC processes is weakened for $m \lesssim 700 \text{ GeV}$ because of the lepton p_T cut we have applied.^{†17} The combined

^{†17}We note here that the sensitivity of the CC processes depends on the lepton p_T cut. For example, adopting the tighter cut, lepton- $p_T > 1 \text{ TeV}$, the CC processes have almost no sensitivity to EWIMPs with $m < 1 \text{ TeV}$. Thus, in particular for the purpose of the Higgsino search, it is important to realize the lepton

results of the NC and CC processes are shown by the solid lines. By combining the two types of processes, the 5σ discovery reaches (95 % C.L. bounds) for Higgsino and Wino are 850 GeV (1.7 TeV) and 1.3 TeV (2.3 TeV), respectively. We find that the combination of the NC and CC processes improves the sensitivity of the EWIMP mass. Furthermore, if we understand all the systematic uncertainties quite well and effectively take the $\sigma_f \rightarrow 0$ limit in the combined result, the detection reach will be pushed up significantly as shown by the dashed lines: 1.1 TeV Higgsino signal at well above 5σ level and a 4σ hint of the 2.9 TeV Wino. These lines should be compared with the combined results and also with those obtained from the conservative analysis with $\sigma_f \rightarrow \infty$, assuming no knowledge about sources of systematic errors. The plot shows us that it is essential to reduce the systematic uncertainties for the detection of EWIMPs through the NC and CC processes.

So far, we have adopted the assumption that the distribution of the nuisance parameters is the Gaussian form and that the fitting function Eq. (5.3) is sufficient for treating systematic errors. In order to discuss the dependence of the results on these assumptions, we have repeated the same analysis using another distribution or fitting function. In the former case, we have adopted the top-hat distribution: the likelihood function for the nuisance parameters L' is given by

$$L'(\boldsymbol{\theta}_f; \boldsymbol{\sigma}_f) \equiv \prod_{\alpha} \Theta \left(\sqrt{3} \sigma_{f,\alpha} - |\theta_{f,\alpha}| \right), \quad (5.12)$$

where Θ is the Heaviside step function. This corresponds to the top-hat distribution of $\theta_{f,\alpha}$ with the variance $\sigma_{f,\alpha}^2$ for each α . As for an example of another fitting function, we have adopted a simple one parameter extension of Eq. (5.3)

$$f_{\text{sys},i}(\boldsymbol{\theta}_f) = e^{\theta_{f,1}} (1 - p_i)^{\theta_{f,2}} p_i^{(\theta_{f,3} + \theta_{f,4} \ln p_i + \theta_{f,5} \ln^2 p_i + \theta_{f,6} \ln^3 p_i)}, \quad (5.13)$$

which consists of six parameters. The variances of the nuisance parameters are estimated in the same way as Sec. 5.2.2, but now with the six parameters.

In Fig. 10, we show the corresponding results. The convention for the line colors is the same as Fig. 9, while the line styles denote different procedures: the dashed and dotted lines correspond to the result with the top-hat distribution and that with the six parameters fitting function, respectively, while solid lines are the same as Fig. 9. From the figure, we can see that the choice of the distribution may slightly affect the result, while the addition of a nuisance parameter as Eq. (5.13) causes almost no effect. The size of the effect of the choice of the distribution for the current estimation of errors σ_f is about 100 GeV (200 GeV) for the 5σ (95 % C.L.) bounds. We expect that such uncertainties due to the procedure to include the systematic errors will be reduced once the data from the real experiment (and hence better understanding of the systematic errors) will become available.

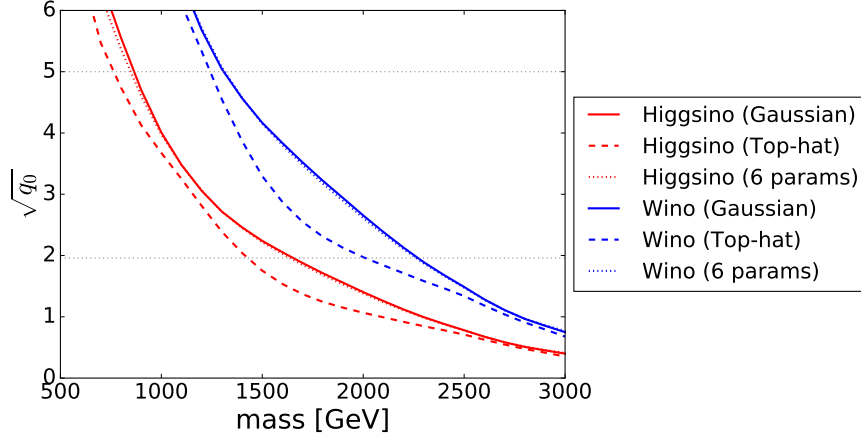


Figure 10: $\sqrt{q_0}$ as a function of the EWIMP mass using both the NC and CC processes. The convention for the line colors is the same as Fig. 9. The line styles denote the result same as Fig. 9 (solid), that with the top-hat distribution (dashed), and that with the six parameters fitting function (dotted).

5.2.4 Determination of EWIMP properties

In this subsection, we show that it is possible to determine the properties of the EWIMPs from the NC and CC processes, thanks to the fact that we can study the $m_{\ell\ell}$ and m_T distribution in great detail for these processes. Some information about the mass, charge, and spin of the EWIMPs can be extracted because the corrections to these distributions from the EWIMPs are completely determined by these EWIMP properties. Firstly, we can extract the EWIMP mass from the position of the dip-like structure in the correction since it corresponds to roughly twice the EWIMP mass as we have shown in Sec. 5.1. Secondly, the overall size of the correction gives us information about the $SU(2)_L$ and $U(1)_Y$ charges. The CC processes depend only on the $SU(2)_L$ charge, while the NC processes depend both on the $SU(2)_L$ and $U(1)_Y$ charges. Consequently, we can obtain information about the gauge charges of the EWIMPs from the NC and CC processes.

We now demonstrate the mass and charge determination of fermionic EWIMPs. This is equivalent to the determination of the parameter set (m, C_1, C_2) . We generate the data assuming the SM + EWIMP model ($\mu = 1$) with some specific values of m, n, Y , and κ , with which we obtain (m, C_1, C_2) . We fix $\mu = 1$ for our theoretical model as well, and hence the theoretical predictions of the number of events also depend on these three parameters, $\mathbf{x}_f = \mathbf{x}_f(m, C_1, C_2)$. We define the likelihood function $L(\tilde{\mathbf{x}}_f; \boldsymbol{\theta}_f, m, C_1, C_2)$ in the same form as Eqs. (5.2) and (5.5) with the theoretical prediction \mathbf{x}_f now understood as a function of

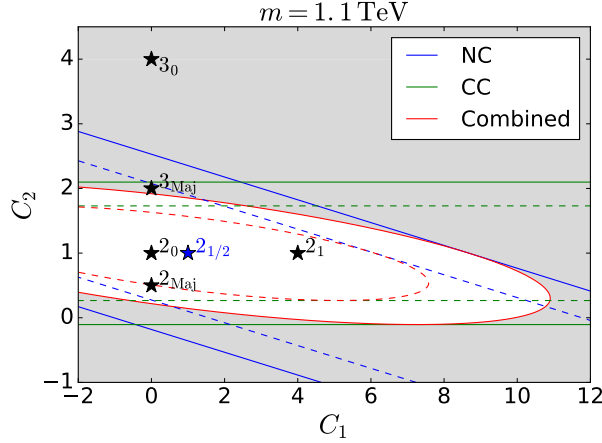


Figure 11: Contour of \sqrt{q} in the C_1 vs. C_2 plane with $m = 1.1$ TeV, where we assume 1.1 TeV Higgsino signal. The dotted and solid lines denote 1σ and 2σ contours, respectively, and the gray region corresponds to the parameter space that is in tension with the observation at more than 2σ level. The blue, green, and red lines correspond to the result from the NC processes, the CC processes, and the combined analysis, respectively. Each star marker annotated as “ n_Y ” represents a point corresponding to a $SU(2)_L$ n -plet Dirac fermion with hypercharge Y , while that with “ n_{Maj} ” corresponds to an $SU(2)_L$ n -plet Majorana fermion.

(m, C_1, C_2) , not of μ .^{‡18} The test statistic is defined as

$$q(m, C_1, C_2) \equiv -2 \sum_f \ln \frac{L(\tilde{\mathbf{x}}_f; \hat{\boldsymbol{\theta}}_f, m, C_1, C_2)}{L(\tilde{\mathbf{x}}_f; \hat{\boldsymbol{\theta}}_f, \hat{m}, \hat{C}_1, \hat{C}_2)}, \quad (5.14)$$

where the parameters $(\{\hat{\boldsymbol{\theta}}_f\}, \hat{m}, \hat{C}_1, \hat{C}_2)$ maximize $\prod_f L(\tilde{\mathbf{x}}_f; \boldsymbol{\theta}_f, m, C_1, C_2)$, while $\hat{\boldsymbol{\theta}}_f$ maximize $L(\tilde{\mathbf{x}}_f; \boldsymbol{\theta}_f, m, C_1, C_2)$ for fixed values of (m, C_1, C_2) . It follows the chi-squared distribution with three degrees of freedom in the limit of a large number of events [4]. The test statistic defined in this way examines the compatibility of a given EWIMP model (i.e. a parameter set (m, C_1, C_2)) with the observed signal.

Once a deviation from the SM prediction is observed in a real experiment, we may determine (m, C_1, C_2) using the above test statistic q . In the following, we show the expected accuracy of the determination of (m, C_1, C_2) for the case where there exists 1.1 TeV Higgsino.^{‡19}

^{‡18}As shown in Eqs. (5.3) and (5.4), C_1 and C_2 are positive quantities (and C_2 is discrete). In the figures, however, we extend the C_1 and C_2 axes down to negative regions just for presentation purposes.

^{‡19}The expected significance is 3.5σ for 1.1 TeV Higgsino in our estimation. Even though it is slightly below the 5σ discovery, we take 1.1 TeV Higgsino as an example because it is a candidate of the thermal relic DM.

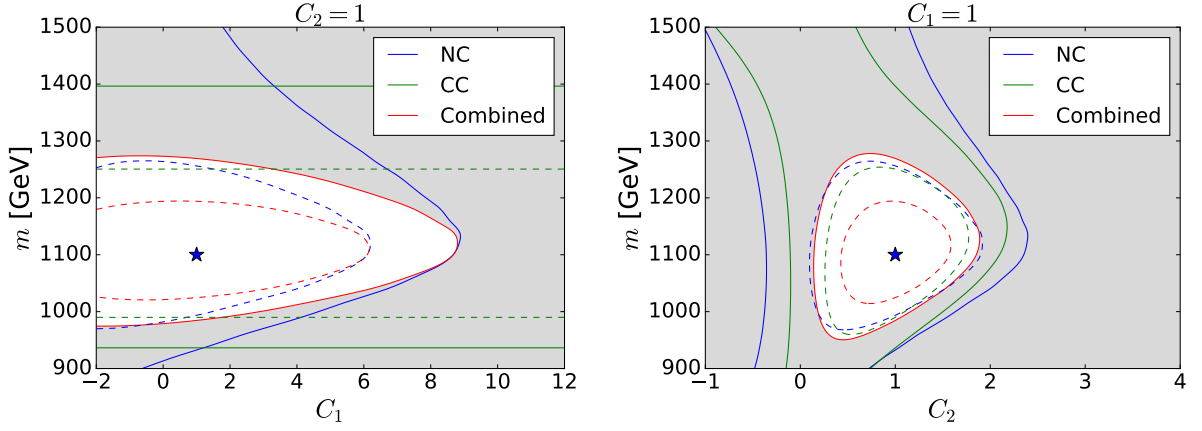


Figure 12: **Left:** Contour of \sqrt{q} in the C_1 vs. m plane with $C_2 = 1$, where we assume the 1.1 TeV Higgsino signal. The colors and styles of lines and the meaning of the gray region are the same as Fig. 11. The star marker corresponds to the true Higgsino property $(C_1, m) = (1, 1.1 \text{ TeV})$. **Right:** Contour of \sqrt{q} in the C_2 vs. m plane for $C_1 = 1$, where we assume the 1.1 TeV Higgsino signal. The star marker corresponds to the true Higgsino property $(C_2, m) = (1, 1.1 \text{ TeV})$.

In Fig. 11, we show the contours of 1σ (dotted) and 2σ (solid) constraints, which correspond to the values $\sqrt{q} = 1.9$ and $\sqrt{q} = 2.8$, respectively, in the C_1 vs. C_2 plane for $m = 1.1 \text{ TeV}$. The blue, green, and red lines denote the result obtained from the NC processes, the CC processes, and the combined analysis, respectively. The models in the gray region are in more than 2σ tension with the observation. We also show several star markers that correspond to the single $SU(2)_L$ multiplet contributions: the markers with “ n_Y ” represent an $SU(2)_L$ n -plet Dirac fermion with hypercharge Y , while those with “ n_{Maj} ” an $SU(2)_L$ n -plet Majorana fermion. Both the NC and CC constraints are represented as straight bands in the C_1 vs. C_2 plane since each process depends on a specific linear combination of C_1 and C_2 . In particular, the CC constraint is independent of C_1 , or Y . In this sense, the NC and CC processes are complementary to each other, and thus we can separately constrain C_1 and C_2 only after combining these two results. For instance, we can exclude a single fermionic $SU(2)_L$ multiplet with $n \neq 2$ at more than 2σ level, although each process by itself cannot exclude the possibility of 3_{Maj} . We can also constrain the hypercharge, yet it is not uniquely determined. In addition to the Higgsino, the EWIMP as an $SU(2)_L$ doublet Dirac fermion with $|Y|^2 \lesssim 2$ or an $SU(2)_L$ doublet Majorana fermion with $|Y|^2 \lesssim 5$ is still allowed.

In Fig. 12, we show the contour plots of \sqrt{q} in the C_1 vs. m plane with $C_2 = 1$ (left) and those in the C_2 vs. m plane with $C_1 = 1$ (right). The star marker in each panel shows the true values of parameters $(C_1, m) = (1, 1.1 \text{ TeV})$ (left) and $(C_2, m) = (1, 1.1 \text{ TeV})$ (right).

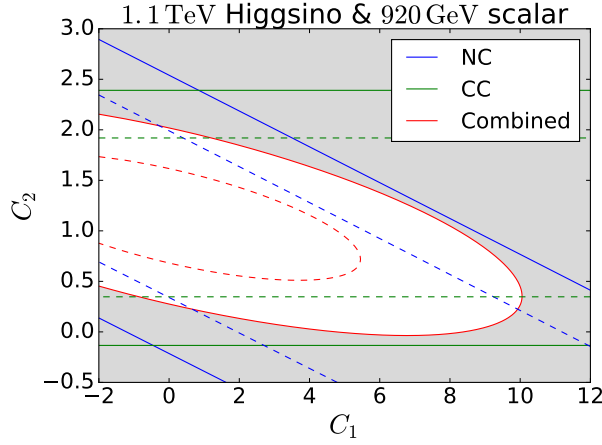


Figure 13: Contour of \sqrt{q} in the C_1 vs. C_2 plane for the 1.1 TeV Higgsino signal, tested with the scalar EWIMP assumption. The plane is defined as the scalar mass of 920 GeV. The colors and styles of lines and the meaning of the gray region are the same as Fig. 11.

Again, by combining the NC and CC results, we can significantly improve the determination of EWIMP properties, making 1σ and 2σ contours closed circles in the planes of our concern. In particular, as red lines show, the combined analysis allows us to determine the observed EWIMP mass at the level of $\mathcal{O}(10)\%$.

Finally, we comment on the possibility of discriminating between fermionic and scalar EWIMPs, whose difference comes from the loop function $f(x)$ (see Eq. (5.2)). Here we repeat the same analysis explained above, assuming the 1.1 TeV Higgsino signal for example, but use the scalar loop function to evaluate the theoretical predictions $\mathbf{x}_f(m, C_1, C_2)$. In Figs. 13 and 14, we show the results in the C_1 vs. C_2 plane and the C_1 (or C_2) vs. m plane, respectively, where one of the three parameters is fixed to its best fit value. It is seen that, in the case of the 1.1 TeV Higgsino signal, it is hard to distinguish between the bosonic and fermionic EWIMPs only with our method. However, if a part of the EWIMP properties (in particular its mass) is determined from another approach, our method may allow us to determine its spin correctly.

We also stress here that, with some favorable assumption about the observed signal, we may obtain some hint about its spin. For example, if we assume that the observed signal composes a fraction of the dark matter in our Universe, the choice of the EWIMP charges is significantly constrained. Note from Fig. 13 that the only choices of EWIMP charges that allow the EWIMP multiplet to contain an electrically neutral component are $(n, |Y|) = (3, 0), (3, 1), (4, 1/2), (4, 3/2)$, and $(5, 0)_{\text{real}}$. The last column of the table 13 shows proper choices of EWIMP masses in order for their thermal relic abundances become comparable with the dark matter abundance in the current Universe. All of those values are somewhat

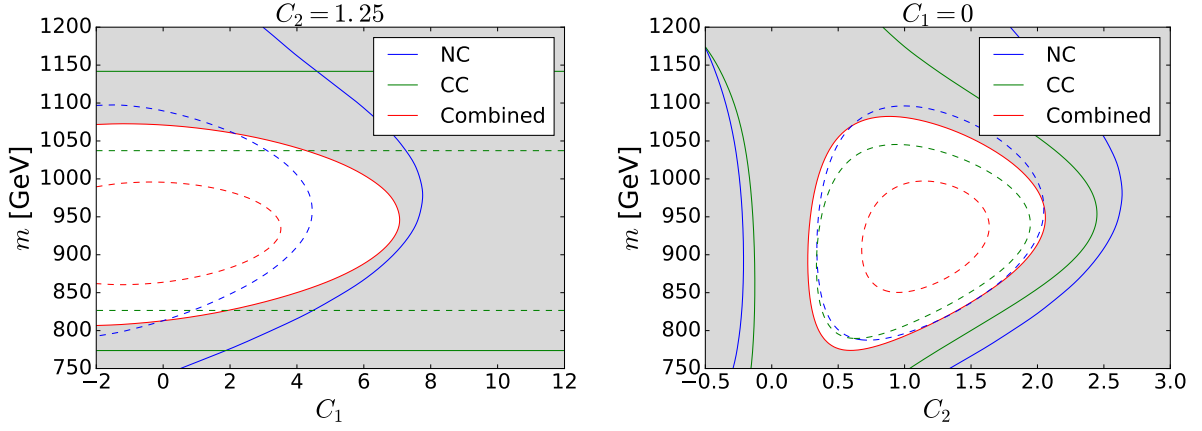


Figure 14: **Left:** Contour of \sqrt{q} in the C_1 vs. m plane with $C_2 = 1.25$ for the 1.1 TeV Higgsino signal, tested with the scalar EWIMP assumption. The colors and styles of lines and the meaning of the gray region are the same as Fig. 11. **Right:** Contour of \sqrt{q} in the C_2 vs. m plane with $C_1 = 0$ for the 1.1 TeV Higgsino signal, tested with the scalar EWIMP assumption.

(n, Y)	C_1	C_2	$m_{\text{DM}}[\text{TeV}]$
$(3, 0)_{\text{real}}$	0	0.25	2.5 [41]
$(3, 0)$	0	0.5	1.55 [43]
$(3, 1)$	0.75	0.5	1.6 [41]
$(4, \frac{1}{2})$	0.25	1.25	2.4 [41]
$(4, \frac{3}{2})$	2.25	1.25	2.9 [41]
$(5, 0)_{\text{real}}$	0	1.25	9.4 [41]

Table 13: The scalar EWIMPs that are compatible with the result in Fig. 13. The observed DM energy density is explained by the thermal relic of the EWIMP with m_{DM} shown in the fourth column.

larger than the central value of the mass of the observed signal, which means that the scalar interpretation of the signal cannot explain the whole of the dark matter relic abundance without introducing some non-thermal production mechanism.

5.3 Conclusion

In this paper, we have discussed the indirect search of EWIMPs at future 100 TeV hadron colliders based on the precision measurement of the production processes of a charged lepton

pair and that of a charged lepton and a neutrino. In particular, we have demonstrated that not only we can discover the EWIMPs, but also we can determine their properties such as their masses, $SU(2)_L$ and $U(1)_Y$ charges, and spins via the processes of our concern. It is based on two facts: the high energy lepton production channel enables us to study its momentum distribution in great detail, and the EWIMP correction shows characteristic features, including a dip-like structure as the final state invariant mass being twice the EWIMP mass. The latter feature also helps us to distinguish the EWIMP signals from backgrounds and systematic errors, as they are not expected to show a dip-like structure. In order to fully exploit the differences between the distributions the EWIMP signals and systematic errors, we have adopted the fitting based analysis as our statistical treatment.

First, we have shown in Fig. 9 the detection reach of Higgsino and Wino from the neutral current (NC) processes (mediated by photon or Z -boson), the charged current (CC) processes (mediated by W -boson), and the combination of these two results. We have seen that the addition of the CC processes improves the detection reach from the previous analysis [79]. From the combined analysis, the bounds at the 5σ (95% C.L.) level for Higgsino and Wino are 850 GeV (1.7 TeV) and 1.3 TeV (2.3 TeV), respectively. This result, in particular that for short lifetime Higgsino, indicates the importance of our method for the EWIMP search.

Next, we have considered the determination of the mass and $SU(2)_L$ and $U(1)_Y$ charges of the observed EWIMP. By combining the NC and the CC events, the position and the height of the dip in the EWIMP effect on the cross section gives us enough information for determining all the three parameters. In Figs. 11 and 12, we have shown the plots of the test statistics that test the validity of several choices of parameters. As a result, the $SU(2)_L$ charge of the observed signal is correctly identified under the assumption of a single EWIMP multiplet, and the $U(1)_Y$ charge and mass are also determined precisely. In order for the determination of the EWIMP spin, we have plotted the contours of the test statistics that test the validity of the scalar EWIMP models with some fixed values of masses and charges. The results are shown in Figs. 13 and 14, which reveals that the spin is not completely determined by solely using our method. Use of another approach to determine the EWIMP properties, or of some assumption like that the observed signal corresponds to the dark matter in our Universe, may help us to obtain further information regarding the EWIMP spin.

Section A

Review of supersymmetry

In this appendix, we briefly review the $\mathcal{N} = 1$ supersymmetry, which is an essential element of the MSSM explained in Sec. ???. Our argument is based on [7, 80].

The $\mathcal{N} = 1$ supersymmetry is

First example is the MSSM, extension of the SM with the so-called $\mathcal{N} = 1$ supersymmetry (SUSY) [7, 80] that relates a bosonic particle and a fermionic particle. The supersymmetry transformations for a complex scalar ϕ and its “superpartner” Weyl fermion ψ are defined as

$$\delta\phi = (\epsilon\psi), \quad \delta\phi^* = (\epsilon^\dagger\psi^\dagger), \quad (\text{A.1})$$

$$\delta\psi = -i(\sigma^\mu\epsilon^\dagger)\partial_\mu\phi, \quad \delta\psi^\dagger = i(\epsilon\sigma^\mu)\partial_\mu\phi^*, \quad (\text{A.2})$$

where $\sigma^\mu \equiv (\mathbf{1}, \boldsymbol{\sigma})$ with $\boldsymbol{\sigma}$ being Pauli matrices, while ϵ is an anti-commuting Weyl fermionic object that parameterizes the SUSY transformation. The summation over the spinor indices is assumed inside each parenthesis. These transformations, if denoted by operators ϵQ and $\epsilon^\dagger Q^\dagger$, are known to form a closed algebra

$$[Q, Q^\dagger] = 2i\sigma^\mu\partial_\mu, \quad (\text{A.3})$$

$$[Q, Q] = [Q^\dagger, Q^\dagger] = 0, \quad (\text{A.4})$$

when fields are on-shell.^{‡20}

^{‡20}In order for the algebra to be closed off-shell, one can introduce a new scalar field F without a kinetic term that is often called as an *auxiliary* field. F works as a Lagrange multiplier whose equation of motion

References

- [1] S. Weinberg, Implications of Dynamical Symmetry Breaking, Phys. Rev. D13 (1976) 974–996, [Addendum: Phys. Rev.D19,1277(1979)]. [doi:10.1103/PhysRevD.19.1277](#), [10.1103/PhysRevD.13.974](#).
- [2] E. Gildener, Gauge Symmetry Hierarchies, Phys. Rev. D14 (1976) 1667. [doi:10.1103/PhysRevD.14.1667](#).
- [3] L. Susskind, Dynamics of Spontaneous Symmetry Breaking in the Weinberg-Salam Theory, Phys. Rev. D20 (1979) 2619–2625. [doi:10.1103/PhysRevD.20.2619](#).
- [4] M. Tanabashi, et al., Review of Particle Physics, Phys. Rev. D98 (3) (2018) 030001. [doi:10.1103/PhysRevD.98.030001](#).
- [5] A. Salam, J. A. Strathdee, On Superfields and Fermi-Bose Symmetry, Phys. Rev. D11 (1975) 1521–1535. [doi:10.1103/PhysRevD.11.1521](#).
- [6] M. T. Grisaru, W. Siegel, M. Rocek, Improved Methods for Supergraphs, Nucl. Phys. B159 (1979) 429. [doi:10.1016/0550-3213\(79\)90344-4](#).
- [7] S. P. Martin, A Supersymmetry primer (1997) 1–98[Adv. Ser. Direct. High Energy Phys.18,1(1998)]. [arXiv:hep-ph/9709356](#), [doi:10.1142/9789812839657_0001](#), [10.1142/9789814307505_0001](#).
- [8] N. Sakai, T. Yanagida, Proton Decay in a Class of Supersymmetric Grand Unified Models, Nucl. Phys. B197 (1982) 533. [doi:10.1016/0550-3213\(82\)90457-6](#).
- [9] G. R. Farrar, P. Fayet, Phenomenology of the Production, Decay, and Detection of New Hadronic States Associated with Supersymmetry, Phys. Lett. 76B (1978) 575–579. [doi:10.1016/0370-2693\(78\)90858-4](#).
- [10] S. Dimopoulos, H. Georgi, Softly Broken Supersymmetry and SU(5), Nucl. Phys. B193 (1981) 150–162. [doi:10.1016/0550-3213\(81\)90522-8](#).
- [11] S. Weinberg, Supersymmetry at Ordinary Energies. 1. Masses and Conservation Laws, Phys. Rev. D26 (1982) 287. [doi:10.1103/PhysRevD.26.287](#).
- [12] S. Dimopoulos, S. Raby, F. Wilczek, Supersymmetry and the Scale of Unification, Phys. Rev. D24 (1981) 1681–1683. [doi:10.1103/PhysRevD.24.1681](#).
- [13] L. O’Raifeartaigh, Spontaneous Symmetry Breaking for Chiral Scalar Superfields, Nucl. Phys. B96 (1975) 331–352. [doi:10.1016/0550-3213\(75\)90585-4](#).

-
- [14] P. Fayet, J. Iliopoulos, Spontaneously Broken Supergauge Symmetries and Goldstone Spinors, *Phys. Lett.* 51B (1974) 461–464. [doi:10.1016/0370-2693\(74\)90310-4](#).
- [15] P. Fayet, Supergauge Invariant Extension of the Higgs Mechanism and a Model for the electron and Its Neutrino, *Nucl. Phys.* B90 (1975) 104–124. [doi:10.1016/0550-3213\(75\)90636-7](#).
- [16] G. F. Giudice, M. A. Luty, H. Murayama, R. Rattazzi, Gaugino mass without singlets, *JHEP* 12 (1998) 027. [arXiv:hep-ph/9810442](#), [doi:10.1088/1126-6708/1998/12/027](#).
- [17] L. Randall, R. Sundrum, Out of this world supersymmetry breaking, *Nucl. Phys.* B557 (1999) 79–118. [arXiv:hep-th/9810155](#), [doi:10.1016/S0550-3213\(99\)00359-4](#).
- [18] T. E. W. Group, 2012 Update of the Combination of CDF and D0 Results for the Mass of the W Boson (2012). [arXiv:1204.0042](#).
- [19] J. Alcaraz, P. Azzurri, A. Bajo-Vaquero, E. Barberio, A. Blondel, D. Bourilkov, P. Checchia, R. Chierici, R. Clare, J. D’Hondt, G. Della Ricca, M. Dierckxsens, D. Duchesneau, G. Duckeck, M. Elsing, M. W. Grünewald, A. Gurtu, J. B. Hansen, R. Hawkings, S. Jezequel, R. W. L. Jones, T. Kawamoto, E. Lançon, W. Liebig, L. Malgeri, S. Mele, M. N. Minard, K. Mönig, C. Parkes, U. Parzefall, B. Pietrzyk, G. Quast, P. B. Renton, S. Riemann, K. Sachs, D. Strom, A. Strässner, R. Tenchini, F. Teubert, M. A. Thomson, S. Todorova-Nová, A. Valassi, A. Venturi, H. Voss, C. P. Ward, N. K. Watson, P. S. Wells, S. Wynhoff, P. de Jong, B. de la Cruz, [A Combination of Preliminary Electroweak Measurements and Constraints on the Standard Model, 2006](#), Tech. Rep. hep-ex/0612034. ALEPH-2006-001 PHYSICS-2006-001. CERN-L3-310. CERN-PH-EP-2006-042. DELPHI-2006-014 PHYS-948. L3-Note-2833. LEPEWWG-2006-01. OPAL-PR-419, CERN, Geneva, preprint not submitted to publication (Dec 2006). URL <https://cds.cern.ch/record/1016509>
- [20] J. Beringer, et al., Review of Particle Physics (RPP), *Phys. Rev.* D86 (2012) 010001. [doi:10.1103/PhysRevD.86.010001](#).
- [21] G. Aad, et al., Measurements of Higgs boson production and couplings in diboson final states with the ATLAS detector at the LHC, *Phys. Lett.* B726 (2013) 88–119, [Erratum: *Phys. Lett.* B734,406(2014)]. [arXiv:1307.1427](#), [doi:10.1016/j.physletb.2014.05.011](#), [10.1016/j.physletb.2013.08.010](#).
- [22] S. Chatrchyan, et al., Measurement of the properties of a Higgs boson in the four-lepton final state, *Phys. Rev.* D89 (9) (2014) 092007. [arXiv:1312.5353](#), [doi:10.1103/PhysRevD.89.092007](#).

- [23] First combination of Tevatron and LHC measurements of the top-quark mass (2014). [arXiv:1403.4427](#).
- [24] V. Tishchenko, et al., Detailed Report of the MuLan Measurement of the Positive Muon Lifetime and Determination of the Fermi Constant, Phys. Rev. D87 (5) (2013) 052003. [arXiv:1211.0960](#), [doi:10.1103/PhysRevD.87.052003](#).
- [25] S. Bethke, World Summary of α_s (2012)[Nucl. Phys. Proc. Suppl.234,229(2013)] (2012). [arXiv:1210.0325](#), [doi:10.1016/j.nuclphysbps.2012.12.020](#).
- [26] D. Buttazzo, G. Degrassi, P. P. Giardino, G. F. Giudice, F. Sala, A. Salvio, A. Strumia, Investigating the near-criticality of the Higgs boson, JHEP 12 (2013) 089. [arXiv:1307.3536](#), [doi:10.1007/JHEP12\(2013\)089](#).
- [27] J. R. Ellis, K. Enqvist, D. V. Nanopoulos, F. Zwirner, Observables in Low-Energy Superstring Models, Mod. Phys. Lett. A1 (1986) 57. [doi:10.1142/S0217732386000105](#).
- [28] R. Barbieri, G. F. Giudice, Upper Bounds on Supersymmetric Particle Masses, Nucl. Phys. B306 (1988) 63–76. [doi:10.1016/0550-3213\(88\)90171-X](#).
- [29] G. F. Giudice, A. Masiero, A Natural Solution to the mu Problem in Supergravity Theories, Phys. Lett. B206 (1988) 480–484. [doi:10.1016/0370-2693\(88\)91613-9](#).
- [30] G. F. Giudice, A. Romanino, Split supersymmetry, Nucl. Phys. B699 (2004) 65–89, [Erratum: Nucl. Phys.B706,487(2005)]. [arXiv:hep-ph/0406088](#), [doi:10.1016/j.nuclphysb.2004.11.048](#), [10.1016/j.nuclphysb.2004.08.001](#).
- [31] J. L. Feng, T. Moroi, Supernatural supersymmetry: Phenomenological implications of anomaly mediated supersymmetry breaking, Phys. Rev. D61 (2000) 095004. [arXiv:hep-ph/9907319](#), [doi:10.1103/PhysRevD.61.095004](#).
- [32] J. L. Feng, K. T. Matchev, T. Moroi, Multi - TeV scalars are natural in minimal supergravity, Phys. Rev. Lett. 84 (2000) 2322–2325. [arXiv:hep-ph/9908309](#), [doi:10.1103/PhysRevLett.84.2322](#).
- [33] J. L. Feng, K. T. Matchev, T. Moroi, Focus points and naturalness in supersymmetry, Phys. Rev. D61 (2000) 075005. [arXiv:hep-ph/9909334](#), [doi:10.1103/PhysRevD.61.075005](#).
- [34] M. Ibe, T. Moroi, T. T. Yanagida, Possible Signals of Wino LSP at the Large Hadron Collider, Phys. Lett. B644 (2007) 355–360. [arXiv:hep-ph/0610277](#), [doi:10.1016/j.physletb.2006.11.061](#).

-
- [35] M. Ibe, T. T. Yanagida, The Lightest Higgs Boson Mass in Pure Gravity Mediation Model, *Phys. Lett. B* 709 (2012) 374–380. [arXiv:1112.2462](#), [doi:10.1016/j.physletb.2012.02.034](#).
 - [36] N. Arkani-Hamed, A. Gupta, D. E. Kaplan, N. Weiner, T. Zorawski, Simply Unnatural Supersymmetry (2012). [arXiv:1212.6971](#).
 - [37] M. Cirelli, N. Fornengo, A. Strumia, Minimal dark matter, *Nucl. Phys. B* 753 (2006) 178–194. [arXiv:hep-ph/0512090](#), [doi:10.1016/j.nuclphysb.2006.07.012](#).
 - [38] M. Cirelli, A. Strumia, M. Tamburini, Cosmology and Astrophysics of Minimal Dark Matter, *Nucl. Phys. B* 787 (2007) 152–175. [arXiv:0706.4071](#), [doi:10.1016/j.nuclphysb.2007.07.023](#).
 - [39] M. Cirelli, A. Strumia, Minimal Dark Matter: Model and results, *New J. Phys.* 11 (2009) 105005. [arXiv:0903.3381](#), [doi:10.1088/1367-2630/11/10/105005](#).
 - [40] M. E. Machacek, M. T. Vaughn, Two Loop Renormalization Group Equations in a General Quantum Field Theory. 1. Wave Function Renormalization, *Nucl. Phys. B* 222 (1983) 83–103. [doi:10.1016/0550-3213\(83\)90610-7](#).
 - [41] M. Farina, D. Pappadopulo, A. Strumia, A modified naturalness principle and its experimental tests, *JHEP* 08 (2013) 022. [arXiv:1303.7244](#), [doi:10.1007/JHEP08\(2013\)022](#).
 - [42] L. Di Luzio, R. Gröber, J. F. Kamenik, M. Nardecchia, Accidental matter at the LHC, *JHEP* 07 (2015) 074. [arXiv:1504.00359](#), [doi:10.1007/JHEP07\(2015\)074](#).
 - [43] E. Del Nobile, M. Nardecchia, P. Panci, Millicharge or Decay: A Critical Take on Minimal Dark Matter, *JCAP* 1604 (04) (2016) 048. [arXiv:1512.05353](#), [doi:10.1088/1475-7516/2016/04/048](#).
 - [44] N. Arkani-Hamed, A. Delgado, G. F. Giudice, The Well-tempered neutralino, *Nucl. Phys. B* 741 (2006) 108–130. [arXiv:hep-ph/0601041](#), [doi:10.1016/j.nuclphysb.2006.02.010](#).
 - [45] J. Hisano, S. Matsumoto, M. Nagai, O. Saito, M. Senami, Non-perturbative effect on thermal relic abundance of dark matter, *Phys. Lett. B* 646 (2007) 34–38. [arXiv:hep-ph/0610249](#), [doi:10.1016/j.physletb.2007.01.012](#).
 - [46] T. Moroi, M. Nagai, M. Takimoto, Non-Thermal Production of Wino Dark Matter via the Decay of Long-Lived Particles, *JHEP* 07 (2013) 066. [arXiv:1303.0948](#), [doi:10.1007/JHEP07\(2013\)066](#).

-
- [47] M. Beneke, A. Bharucha, F. Dighera, C. Hellmann, A. Hryczuk, S. Recksiegel, P. Ruiz-Femenia, Relic density of wino-like dark matter in the MSSM, JHEP 03 (2016) 119. [arXiv:1601.04718](#), [doi:10.1007/JHEP03\(2016\)119](#).
- [48] F. Zwicky, Die Rotverschiebung von extragalaktischen Nebeln, Helvetica Physica Acta 6 (1933) 110.
- [49] F. Zwicky, On the Masses of Nebulae and of Clusters of Nebulae, Astrophysical Journal 86 (1937) 217.
- [50] V. Trimble, Existence and Nature of Dark Matter in the Universe, Ann. Rev. Astron. Astrophys. 25 (1987) 425–472. [doi:10.1146/annurev.aa.25.090187.002233](#).
- [51] H. W. Babcock, The rotation of the Andromeda Nebula, Lick Observatory Bulletin 19 (1939) 41–51. [doi:10.5479/ADS/bib/1939LicOB.19.41B](#).
- [52] K. G. Begeman, A. H. Broeils, R. H. Sanders, Extended rotation curves of spiral galaxies: Dark haloes and modified dynamics, Mon. Not. Roy. Astron. Soc. 249 (1991) 523.
- [53] G. Jungman, M. Kamionkowski, A. Kosowsky, D. N. Spergel, Weighing the universe with the cosmic microwave background, Phys. Rev. Lett. 76 (1996) 1007–1010. [arXiv:astro-ph/9507080](#), [doi:10.1103/PhysRevLett.76.1007](#).
- [54] G. Jungman, M. Kamionkowski, A. Kosowsky, D. N. Spergel, Cosmological parameter determination with microwave background maps, Phys. Rev. D54 (1996) 1332–1344. [arXiv:astro-ph/9512139](#), [doi:10.1103/PhysRevD.54.1332](#).
- [55] N. Aghanim, et al., Planck 2018 results. VI. Cosmological parameters (2018). [arXiv:1807.06209](#).
- [56] P. Gondolo, G. Gelmini, Cosmic abundances of stable particles: Improved analysis, Nucl. Phys. B360 (1991) 145–179. [doi:10.1016/0550-3213\(91\)90438-4](#).
- [57] G. Belanger, F. Boudjema, A. Pukhov, A. Semenov, MicrOMEGAs: A Program for calculating the relic density in the MSSM, Comput. Phys. Commun. 149 (2002) 103–120. [arXiv:hep-ph/0112278](#), [doi:10.1016/S0010-4655\(02\)00596-9](#).
- [58] G. Bélanger, F. Boudjema, A. Goudelis, A. Pukhov, B. Zaldivar, micrOMEGAs5.0 : Freeze-in, Comput. Phys. Commun. 231 (2018) 173–186. [arXiv:1801.03509](#), [doi:10.1016/j.cpc.2018.04.027](#).
- [59] J. Hisano, S. Matsumoto, M. M. Nojiri, O. Saito, Non-perturbative effect on dark matter annihilation and gamma ray signature from galactic center, Phys. Rev. D71 (2005) 063528. [arXiv:hep-ph/0412403](#), [doi:10.1103/PhysRevD.71.063528](#).

-
- [60] M. Benedikt, M. Capeans Garrido, F. Cerutti, B. Goddard, J. Gutleber, J. M. Jimenez, M. Mangano, V. Mertens, J. A. Osborne, T. Otto, J. Poole, W. Riegler, D. Schulte, L. J. Tavian, D. Tommasini, F. Zimmermann, **Future Circular Collider**, Tech. Rep. CERN-ACC-2018-0058, CERN, Geneva, submitted for publication to Eur. Phys. J. ST. (Dec 2018).
URL <https://cds.cern.ch/record/2651300>
- [61] M. Ahmad, et al., CEPC-SPPC Preliminary Conceptual Design Report. 1. Physics and Detector (2015).
- [62] C.-S. S. Group, CEPC-SPPC Preliminary Conceptual Design Report. 2. Accelerator (2015).
- [63] D. Binosi, J. Collins, C. Kaufhold, L. Theussl, **Jaxodraw: A graphical user interface for drawing feynman diagrams. version 2.0 release notes**, Computer Physics Communications 180 (9) (2009) 1709 – 1715. doi:<https://doi.org/10.1016/j.cpc.2009.02.020>.
URL <http://www.sciencedirect.com/science/article/pii/S0010465509000757>
- [64] J. Vermaseren, **Axodraw**, Computer Physics Communications 83 (1) (1994) 45 – 58. doi:[https://doi.org/10.1016/0010-4655\(94\)90034-5](https://doi.org/10.1016/0010-4655(94)90034-5).
URL <http://www.sciencedirect.com/science/article/pii/0010465594900345>
- [65] J. Alwall, M. Herquet, F. Maltoni, O. Mattelaer, T. Stelzer, MadGraph 5 : Going Beyond, JHEP 06 (2011) 128. [arXiv:1106.0522](#), doi:[10.1007/JHEP06\(2011\)128](https://doi.org/10.1007/JHEP06(2011)128).
- [66] J. Alwall, R. Frederix, S. Frixione, V. Hirschi, F. Maltoni, O. Mattelaer, H. S. Shao, T. Stelzer, P. Torrielli, M. Zaro, The automated computation of tree-level and next-to-leading order differential cross sections, and their matching to parton shower simulations, JHEP 07 (2014) 079. [arXiv:1405.0301](#), doi:[10.1007/JHEP07\(2014\)079](https://doi.org/10.1007/JHEP07(2014)079).
- [67] T. Sjöstrand, S. Ask, J. R. Christiansen, R. Corke, N. Desai, P. Ilten, S. Mrenna, S. Prestel, C. O. Rasmussen, P. Z. Skands, An Introduction to PYTHIA 8.2, Comput. Phys. Commun. 191 (2015) 159–177. [arXiv:1410.3012](#), doi:[10.1016/j.cpc.2015.01.024](https://doi.org/10.1016/j.cpc.2015.01.024).
- [68] J. de Favereau, C. Delaere, P. Demin, A. Giammanco, V. Lemaître, A. Mertens, M. Selvaggi, DELPHES 3, A modular framework for fast simulation of a generic collider experiment, JHEP 02 (2014) 057. [arXiv:1307.6346](#), doi:[10.1007/JHEP02\(2014\)057](https://doi.org/10.1007/JHEP02(2014)057).
- [69] M. L. Mangano, M. Moretti, F. Piccinini, M. Treccani, Matching matrix elements and shower evolution for top-quark production in hadronic collisions, JHEP 01 (2007) 013. [arXiv:hep-ph/0611129](#), doi:[10.1088/1126-6708/2007/01/013](https://doi.org/10.1088/1126-6708/2007/01/013).

-
- [70] R. D. Ball, V. Bertone, S. Carrazza, L. Del Debbio, S. Forte, A. Guffanti, N. P. Hartland, J. Rojo, Parton distributions with QED corrections, Nucl. Phys. B877 (2013) 290–320. [arXiv:1308.0598](#), [doi:10.1016/j.nuclphysb.2013.10.010](#).
- [71] S. Asai, S. Chigusa, T. Kaji, T. Moroi, M. Saito, R. Sawada, J. Tanaka, K. Terashi, K. Uno, Studying gaugino masses in supersymmetric model at future 100 TeV pp collider, JHEP 05 (2019) 179. [arXiv:1901.10389](#), [doi:10.1007/JHEP05\(2019\)179](#).
- [72] M. Aaboud, et al., Search for a new heavy gauge boson resonance decaying into a lepton and missing transverse momentum in 36 fb^{-1} of pp collisions at $\sqrt{s} = 13\text{ TeV}$ with the ATLAS experiment, Eur. Phys. J. C78 (5) (2018) 401. [arXiv:1706.04786](#), [doi:10.1140/epjc/s10052-018-5877-y](#).
- [73] A. M. Sirunyan, et al., Search for high-mass resonances in final states with a lepton and missing transverse momentum at $\sqrt{s} = 13\text{ TeV}$, JHEP 06 (2018) 128. [arXiv:1803.11133](#), [doi:10.1007/JHEP06\(2018\)128](#).
- [74] T. Aaltonen, et al., Search for new particles decaying into dijets in proton-antiproton collisions at $s^{*}(1/2) = 1.96\text{-TeV}$, Phys. Rev. D79 (2009) 112002. [arXiv:0812.4036](#), [doi:10.1103/PhysRevD.79.112002](#).
- [75] G. Cowan, K. Cranmer, E. Gross, O. Vitells, Asymptotic formulae for likelihood-based tests of new physics, Eur. Phys. J. C71 (2011) 1554, [Erratum: Eur. Phys. J.C73,2501(2013)]. [arXiv:1007.1727](#), [doi:10.1140/epjc/s10052-011-1554-0](#), [10.1140/epjc/s10052-013-2501-z](#).
- [76] A. Buckley, J. Ferrando, S. Lloyd, K. Nordström, B. Page, M. Rüfenacht, M. Schönherr, G. Watt, LHAPDF6: parton density access in the LHC precision era, Eur. Phys. J. C75 (2015) 132. [arXiv:1412.7420](#), [doi:10.1140/epjc/s10052-015-3318-8](#).
- [77] L. Di Luzio, R. Gröber, G. Panico, Probing new electroweak states via precision measurements at the LHC and future colliders, JHEP 01 (2019) 011. [arXiv:1810.10993](#), [doi:10.1007/JHEP01\(2019\)011](#).
- [78] S. Matsumoto, S. Shirai, M. Takeuchi, Indirect Probe of Electroweak-Interacting Particles with Mono-Lepton Signatures at Hadron Colliders (2018). [arXiv:1810.12234](#).
- [79] S. Chigusa, Y. Ema, T. Moroi, Probing electroweakly interacting massive particles with Drell-Yan process at 100 TeV hadron colliders, Phys. Lett. B789 (2019) 106–113. [arXiv:1810.07349](#), [doi:10.1016/j.physletb.2018.12.011](#).

-
- [80] J. Wess, J. A. Bagger, *Supersymmetry and supergravity; 2nd ed.*, Princeton Series in Physics, Princeton Univ. Press, Princeton, NJ, 1992.
URL <https://cds.cern.ch/record/320631>